Mouse models of human *PIK3CA*-related brain overgrowth have acutely treatable epilepsy

Achira Roy[1], Jonathan Skibo[1], Franck Kalume[1], Jing Ni[2], Sherri Rankin[3], Yiling Lu[4], William B. Dobyns[1], Gordon B. Mills[4], Jean J. Zhao[2], Suzanne J. Baker[3], Kathleen J. Millen[1]*

[1]Center for Integrative Brain Research, Seattle Children's Research Institute, Seattle, Washington 98101, USA; [2]Department of Cancer biology, Dana Farber Cancer Institute, Boston, Massachusetts 02215, USA; [3]Department of Developmental Neurobiology, St. Jude Children's Research Hospital, Memphis, Tennessee 38105, USA; [4]The University of Texas MD Anderson Cancer Center, Houston, TX 77030

*Correspondence: Kathleen J Millen
Seattle Children's Research Institute
JMB 10 - Center for Integrative Brain Research
1900 9th Avenue
Seattle, WA 98101
Email:kathleen.millen@seattlechildrens.org
Tel: +1-206-884-3225

Competing Interests Statement: All authors read and approved the final manuscript. None of the authors have competing interests.

Short Title: PIK3CA mice model brain overgrowth and epilepsy

Keywords: PI3K; megalencephaly; mouse models; epilepsy; BKM120; cortical dysplasia

Number of Figures: 8

Number of Figure supplements: 12

Number of tables: 1

ABSTRACT

Mutations in the catalytic subunit of phosphoinositide 3-kinase (*PIK3CA)* and other PI3K-AKT pathway components have been associated with cancer and a wide spectrum of brain and body overgrowth. In the brain, the phenotypic spectrum of *PIK3CA*-related segmental overgrowth includes bilateral dysplastic megalencephaly, hemimegalencephaly and focal cortical dysplasia, the most common cause of intractable pediatric epilepsy. We generated mouse models expressing the most common activating *Pik3ca* mutations (*H1047R* and *E545K*) in developing neural progenitors. These accurately recapitulate all the key human pathological features including brain enlargement, cortical malformation, hydrocephalus and epilepsy, with phenotypic severity dependent on the mutant allele and its time of activation. Underlying mechanisms include increased proliferation, cell size and altered white matter. Notably, we demonstrate that acute 1hour-suppression of PI3K signaling despite the ongoing presence of dysplasia has dramatic anti-epileptic benefit. Thus PI3K inhibitors offer a promising new avenue for effective anti-epileptic therapy for intractable pediatric epilepsy patients.

INTRODUCTION

The phosphoinositide-3 kinase (PI3K)-AKT pathway is a central player of intracellular signaling, conserved from yeast to mammals. Activating mutations in genes of PI3K-AKT signaling pathway, especially *PIK3CA*, encoding the catalytic p110α isoform of the PI3K complex, have long been linked to cancer[1-6]. Germline and mosaic mutations of *PIK3CA* and other pathway genes also cause a wide range of brain and body overgrowth disorders; all anomalies caused by somatic *PIK3CA* mutations are now collectively termed *PIK3CA*-Related Overgrowth Spectrum (PROS)[7]. The broad spectrum of brain overgrowth disorders caused by *PIK3CA* activating mutations is impressive. Three strongly activating *PIK3CA* mutations found most commonly in cancer (hotspot mutations) result in severe segmental cortical dysplasia (SEGCD), which includes bilateral dysplastic megalencephaly (MEG), hemimegalencephaly (HMEG) and focal cortical dysplasia (FCD) types 2a/2b[8-11]. Other mutations, resulting in intermediate or weak *PIK3CA* activation, cause MEG or MEG with polymicrogyria (MEG-PMG) as part of the MEG-capillary malformation syndrome (MCAP)[10,12,13]. Developmental features of these brain disorders include cortical malformations, hydrocephalus, Chiari malformation, intellectual disability, autism and epilepsy[7,12]. FCD represents one of the most common causes of intractable epilepsy[14-16].

Conditional mouse alleles for the *H1047R* and *E545K Pik3ca* hotspot mutations have been generated to study tumor formation and assess anti-cancer activities of pathway inhibitors[17-21]. To understand the cellular mechanisms behind *PIK3CA*-related brain overgrowth disorders, we used a series of *cre*-drivers to activate expression of *H1047R* and *E545K* alleles in subsets of neural progenitors. Dramatic phenotypes

resulted, faithfully modeling the entire spectrum of *PIK3CA*-associated human brain disorders including enlarged brain size, hydrocephalus, cortical dysplasia and epilepsy. The severity of these brain phenotypes critically depended on the *Pik3ca* allele and its time of activation. Notably, *Pik3ca*-associated epilepsy in mice was independent of brain overgrowth and cortical dysplasia. Further the seizures of adult megalencephalic mice were suppressed by acute 1hour-administration of pan-PI3K inhibitor BKM120[22]. We conclude that epilepsy in these models represents an active *Pik3ca*-driven process that can be restricted by dynamic modulation of PI3K pathway activity in dysmorphic brains. These results raise the exciting prospect of new molecular based epilepsy therapies in patients whose seizures have been intractable to current anti-seizure therapies.

RESULTS

Megalencephaly caused by Pik3ca overactivation is dependent on both the nature of the mutant allele and its time of overactivation

Two conditional *Pik3ca* activating alleles (*H1047R* and *E545K)* were crossed with *cre*-drivers to overactivate p110α in progressively restricted sets of neural progenitors and their progeny. The broadest distribution was achieved with *Nestin-cre*, being expressed in nearly all neural progenitors from early embryonic stages. A subset of late embryonic progenitors was targeted by *hGFAP-cre*; while tamoxifen-inducible *Nestin-creER* line drove *cre*-expression in a small subset of neural progenitors around birth. Expression of *H1047R* was dependent upon a tri-allelic system with tet-inducible mutant human cDNA activated by cre-dependent expression of the tet-activator protein[18] (**Figure 1 – figure supplement 1**). The *E545K* mutation was knocked into the endogenous *Pik3ca* locus and a lox-stop-lox cassette introduced upstream of the initiation-coding exon, rendering the mutant allele cre-dependent[20]. The activity of all cre drivers was confirmed using reporter lines **(Figure 1 – figure supplement 2)**.

The most severe phenotype was achieved in *hGFAP-cre*;*H1047R* mutants, when doxycycline was administered from embryonic day (E)0.5. All mutants exhibited progressive hydrocephalus and died prior to weaning. Hydrocephalus was evident as a domed forehead at postnatal day (P)21 (**Figure 1b**). Hematoxylin-eosin stained P3 sections showed ventriculomegaly in the megalencephalic *H1047R* mutant brains. Strikingly the hippocampus was not evident in these mutants. Instead, the medial tissue was highly dysplastic with multiple infoldings along its entire length (**Figure 1c,d**). In contrast, when pups were treated with doxycycline from P1, no morphological

differences were observed between the control and the *hGFAP-cre*;*H1047R* mutant **(Figure 1 – figure supplement 3)**. Thus the effect of *H1047R* mutation on brain size was dependent on time of activation.

E545K mice with the same *cre*-driver (*hGFAP-cre;E545K)* had a milder phenotype, surviving as adults without hydrocephalus, though their brain size was significantly larger compared to control littermates (**Figure 1e,h,j**). This provides evidence that with identical time of activation by the same cre driver, the brain phenotypes are dependent on specific *Pik3ca* allele. Earlier activation of *E545K* mutation with *Nestin-cre* led to an even more striking 54.4% volumetric increase, with mild ventriculomegaly and no hydrocephalus (**Figure 1f,h,k**). Interestingly, neonatal activation of *E545K* using *Nestin-creER* had no apparent impact on brain size (**Figure 1g,h,l**). Enlarged head size in both *Nestin-cre;E545K* and *hGFAP-cre;E545K* mutants was evident at birth and brain size of all the three adult E545K mutants was relatively stable (data not shown). Unlike *H1047R* mutants, gross morphology was normal for all *E545K* mutants. We conclude that brain phenotypes caused by Pik3ca-overactivation are both allele and time dependent. Further, we conclude that to cause brain overgrowth, overactivation of Pik3ca function is required during embryogenesis.

Multiple allele-dependent embryonic mechanisms drive *Pik3ca*-MEG

To assess the mechanisms causing Pik3ca-dependent embryonic brain enlargement, we focused our analysis on *hGFAP-cre;H1047R* (doxycycline from E0.5) and *Nestin-cre;E545K* mutants, since these allelic combinations had the most extreme megalencephalic phenotypes.

The inner cortical length of *hGFAP-cre;H1047R* mutants was longer than controls at both E14.5 ($p<0.01$) and E16.5 ($p<0.001$; **Figure 2b-g**). This was accompanied by enlarged nuclear and cell size at both ages and decreased cell density at E16.5, but not increased proliferation or cell cycle exit (**Figure 3c-l**). Total cell number per cortical column length was not significantly different between control and *H1047R* mutant both at E14.5 and E16.5. Also, $TUNEL^+$ cell number was significantly lower in E16.5 mutant cortex than in control ($p<0.01$), indicating reduced apoptosis (**Figure 3 – figure supplement 1 a,c**); however the overall TUNEL+ cell numbers for both control and mutant were small. Together these results indicate that cortical expansion in *hGFAP-cre;H1047R* mutant was not primarily driven by increased proliferation or reduced apoptosis; rather reduced cell density and increased cell size during embryogenesis were major contributing factors.

By contrast, in *Nestin-cre;E545K* mutants, the inner cortical length was comparable to controls at E14.5 but elongated at E16.5 ($p<0.01$); cortical thickness was slightly reduced in E16.5 ($p<0.05$) as compared to controls (**Figure 2h-m**). The labeling index was similar to the control at E14.5 but increased in E16.5 mutants ($p<0.05$), indicating more proliferation (**Figure 3m,o,r**). Cell density in *E545K* mutant neocortex was similar to the control at E14.5 but was reduced at E16.5 ($p<0.05$). Total cells per cortical column length did not change in the *E545K* mutant; but the $TUNEL^+$ cell number was lower in E16.5 mutant cortex than in control ($p<0.001$). Intriguingly, the nuclear size of these mutant cells was similar to controls at both E14.5 and E16.5 but cell somas were significantly larger ($p<0.05$) at E16.5 (**Figure 3n,p,q,s,t**). The quit fraction indicative of rate of cells exiting cell cycle was significantly higher ($p<0.05$) in the *E545K*

mutant between E15.5 and E16.5 (**Figure 3u,v**). At P35, *Nestin-cre;E545K* mutant neocortical cells were still larger ($p<0.05$) compared to controls (**Figure 3 – figure supplement 2a,b**). Notably, in adult P35 E545K*Nestin-creER;E545K* animals where activation was initiated in neonates, and brain size was not different from controls, *E545K*-activated (YFP+) cells have the same size as controls (**Figure 3 – figure supplement 2c,d**). We conclude that increased cell size due to *E545K* overactivation also has a critical embryonic period. Further, changes in multiple developmental parameters including proliferation, cell cycle exit, cell size and density contribute to MEG of *Nestin-cre;E545K Pik3ca* embryonic overactivation.

Embryonic *Pik3ca* activation results in cortical dysplasia

Since disordered lamination is a key feature of human SEGCD[23,24], we assessed neocortical organization and development in both *hGFAP-cre;H1047R* and *Nestin-cre;E545K* mutants. First, we studied the effect of *Pik3ca* overactivation on the Nestin-positive radial glial fibers, the scaffold for glial-guided neuronal migration, at multiple developmental stages. In *H1047R* mutants, the radial glial scaffold was slightly fasciculated and irregular at E14.5 and E16.5. Irregularities were very prominent at P0 when a disrupted pial surface was associated with irregular clusters of enlarged radial glial end-feet (**Figure 4 – figure supplement 1**). The radial glial phenotype was much more subtle in the *E545K* mutant at E14.5 and E16.5; however at P0, we observed thinning of radial glial fibers and irregular clusters of end-feet at the intact pial surface (**Figure 5 – figure supplement 1**).

Cajal-Retzius cells expressing Reelin, a major regulator of radial migration, were normally present in an ordered array in the marginal zone (layer I) of controls and

Nestin-cre;E545K mice (**Figure 4b; Figure 5b,c**). However, these cells were dysplastic in *hGFAP-cre;H1047R* mice at E16.5 (**Figure 4c,c'**). We did not observe ectopic Reelin-positive cells within the cortical column in either mutant. As expected, within the developing wildtype neocortex, Ctip2 and Tbr1 were expressed predominantly in the early-born, deep layers (layers V-VI), while Cux1 was expressed in late-born upper layers (layers II-IV). *hGFAP-cre;H1047R* mutants displayed a marked disorganization of all layers. Ctip2/Tbr1-positive as well as $Cux1^+$ cells in the E16.5 *H1047R* mutant were dispersed throughout the cortical plate, with both early- and late-born neurons severely mislocalized (**Figure 4d-g**). Laminar disorganization was less severe in E16.5 *Nestin-cre;E545K brains*, but deep Ctip2/Tbr1-positive neurons and upper $Cux1^+$ neurons were dispersed throughout the cortical plate (**Figure 5f,g**).

Laminar patterns in postnatal animals remained disrupted in both mutants, with *hGFAP-cre;H1047R* cortex more affected *Nestin-cre;E545K* mutant cortex (**Figure 5h-m**). Thus a simple developmental delay was not the cause of dysplasia (**Figure 4h-m; Figure 5h-m**). In P3 *hGFAP-cre;H1047R* mutants, NeuN-positive mature cortical neurons were found within the normally cell-sparse marginal zone as well as in the cortical white matter and residual ventricular zone, a feature reported in SEGCD patients[23]. Further, the cortical subplate was not readily discernible in these mutants (**Figure 4h-k; Figure 4 – figure supplement figure 2e,f**), blurring the boundary between grey and white matter – a feature often observed in SEGCD patients[24].

To determine whether the mislocalization of neocortical cells was due to defects in cell fate specification and/or migration, we labeled cells at either E12.5 or at E16.5 with pulse of BrdU and assessed cortical neuronal location and fate (layer V; $Ctip2^+$ and

layers II/III; Cux1$^+$) (**Figure 6a**). The total numbers of BrdU$^+$ P0 cells, born at E12.5 and E16.5, were not significantly different between controls and either *hGFAP-cre;H1047R* or *Nestin-cre;E545K* mutants (**Figure 6b,j**). The distribution of BrdU$^+$ cells showed significant differences between controls and *H1047R* mutants labelled during both early and late embryonic stages. At P0, more BrdU$^+$ cells were localized in the lower cortical plate (CP) and white matter (**Figure 6c**). For *E545K* mutants the BrdU$^+$ cell numbers were not different at either age. The distribution was subtly, yet significantly different only for the early born neurons (**Figure 6k**). For both the *H1047R* and *E545K Pik3ca* activating alleles, total layer V (Ctip2$^+$) cell numbers at P0 were not significantly different between controls and mutants (**Figure 6d,l**). Also, the numbers of Ctip2/BrdU double-labeled cells were the same in controls and mutants, indicating that cell fate specification for these deep layer neurons was unaffected by either the *H1047R* or *E545K Pik3ca* allele (**Figure 6e,m**). However, similar to the overall BrdU$^+$ cell distribution, the specific distribution of layer V neurons was abnormal in *H1047R* mutants, with ectopic Ctip2/BrdU double-labeled cells in the upper and lower CP and white matter, instead of mid CP (**Figure 6f**). In *E545K* mutants, fewer Ctip2$^+$ cells were positioned in the mid CP (**Figure 6n**), although the phenotype was much less severe.

Upper layer (Cux1$^+$) neuronal numbers and distributions were significantly different in both *H1047R* and *E545K* mutants, compared to their respective controls (**Figure 6g,o**). In *E545K* mutants, the increase in total Cux1$^+$ cell numbers in the *E545K* mutant corresponded to increased Cux1/BrdU double-labeled cells, born at E16.5 (**Figure 6p**). However, no such correlation was observed in E12.5 or E16.5-born Cux1$^+$ cells in the *H1047R* mutant (**Figure 6h**). These extra cells were therefore likely born

between E16.5 and P0. The distribution of $Cux1^+$ cells was disrupted in both mutants, with the *H1047R* mutant displaying the more severe phenotype (**Figure 6i,q**). Together, these data indicate that cell fates are largely correctly specified in both *Pik3ca* mutants and that cortical dysplasia is more likely caused by aberrant neuronal migration.

***Pik3ca* mutations cause white matter dysplasia**

In P3 *hGFAP-cre;H1047R* mutants, although the cortical plate itself was not dramatically thicker than controls, the underlying cortical white matter was much thicker (**Figure 4j,k; Figure 4 – figure supplement 2e,f**). This was less pronounced but readily discernible in P3 *Nestin-cre;E545K* mutants (**Figure 5 – figure supplement 2c,d**). In P3 *H1047R mutants*, there was complete absence of corpus callosum, although hippocampal and anterior commissures were present (**Figure 4 – figure supplement 1a-d**). In contrast, all major tracts were present in P3 *E545K* mutants (**Figure 5 – figure supplement 2**). These data are consistent with the wide spectrum of white matter dysplasia reported in MEG and SEGCD patients[10,25-27]. Moreover, increased number of Olig2-positive cells was observed in the white matter area of both *H1047R* and *E545K* mutants (**Figure 4 – figure supplement 2, Figure 5 – figure supplement 2**). Although astrocytosis is observed when mTOR signaling is activated by TSC mutations in humans and mice[28,29], it is not a feature of PIK3CA-pathology in our mouse models (**Figure 5 – supplement 3a-d**).

Both megalecephalic and normocephalic *E545K* mutant mice are epileptic

Epilepsy is one of the most important clinical features of SEGCD[14-16,23]. Since most of the *H1047R* mutants were not viable post-weaning, we assessed *Nestin-*

cre;E545K (megalencephalic) and *Nestin-creER;E545K* (normocephalic) adults for epilepsy phenotypes. Baseline sleep EEG recordings in both animal models revealed epileptiform activity including sets of spikes/polyspikes, and regional and generalized spike and wave discharges during non-rapid eye movement (NREM) sleep (**Figure 7b,c**). We also conducted additional two hours of continuous EEG recording immediately after five hours of total sleep deprivation of the *Nestin-creER;E545K* mice. Sleep deprivation is commonly implemented during epilepsy diagnostic studies in mice and humans and increases the sensitivity and specificity of EEG diagnosis for epilepsy[26,30-32]. The frequency of epileptiform interictal activity was increased in post sleep deprivation EEG recordings, and clinically relevant spontaneous seizures including myoclonic (MC) seizures, frequent isolated spikes, and train of spikes, were observed in the *Nestin-creER;E545K* mice (**Figure 7d,e**).

When challenged with the chemoconvulsant pentylenetetrazol (PTZ), a GABA-A receptor antagonist[33], both the megalencephalic and normocephalic *E545K* mouse models exhibited lower seizure thresholds compared to controls at both P35 and P180 (**Figure 7f-i; Figure 7 – figure supplement 1d**). In the 30 min post PTZ injection, both models showed shorter latencies to first generalized tonic clonic (GTC) seizures, more myoclonic seizures, and a prolonged seizure load.

We conclude that *Pik3ca* overactivation is sufficient to cause epilepsy. Further our data indicate that *Pik3ca*-related epilepsy is dissociable from brain overgrowth and cortical dysplasia.

Acute inhibition of Pik3ca activity suppresses epilepsy, rapidly altering cell signaling

BKM120, a 2,6-dimorpholino pyrimidine derivative, is an orally available pan-Class I PI3K inhibitor currently in clinical trials for solid tumors[22,34,35] and may represent a novel therapeutic agent for *PIK3CA*-related epilepsy. Preclinical studies show that BKM120 maximally inhibits downstream phosphorylation of Akt 1hr post-administration[22]. To test its anti-seizure effects in our adult *Pik3ca*^{E545K} gain-of-function megalencephalic and normocephalic models, we administered 50 mg/kg BKM120[22] by oral gavage 1hr prior to PTZ-challenge at ~P35. BKM120 increased the seizure threshold of control animals. More importantly, despite the presence of megalencephaly and considerable cortical dysplasia in P35 *Nestin-cre;E545K* megencephalic animals, BKM120 dramatically decreased the seizure number and duration to untreated control levels and marginally increased seizure latency in the mutant mice (**Figure 7h,i; Figure 7 – figure supplement 1d**). These data powerfully demonstrate that dynamic Pik3ca-dependent processes, independent of cortical and cellular dysplasia cause *Pik3ca*-related epilepsy and they are highly amenable to therapeutic intervention.

To begin to dissect the cell signaling mechanisms underlying Pik3ca-driven epilepsy, we conducted reverse phase protein array (RPPA) analysis to measure protein levels of a comprehensive panel of cell signaling molecules[36]. We assessed subdissected cortical and hippocampal tissue from untreated (-) and PTZ, BKM120 and BKM120+PTZ treated adult control and *Nestin-cre;E545K* mutants (**Figure 8, Figure 8 – figure supplement 1**). As expected, untreated *Nestin-cre;E545K* mutants exhibited significant elevations of phospho (p)S473-Akt and pT346-NDRG1, consistent with PI3K

pathway activation. Notably, baseline pS473-Akt levels in the *Nestin-cre;E545K* hippocampus were prominently higher than the cortical levels. In both *E545K* mutant and control brain tissues, PTZ treatment alone increased the levels of pAkt, especially pS473-Akt, of pS6 (pS235/S236, pS240/244), pT346-NDRG1 and pS2448-mTOR. As expected, acute BKM120 treatment alone reduced phosphorylation of multiple PI3K pathway members, including AKT, S6, NDRG1, GSK3 and 4EBP1. Most remarkably, BKM120 also inhibited the increased phosphorylation levels induced by PTZ, notably returning mutant hippocampal pS473-AKT levels to baseline untreated control levels.

DISCUSSION

PIK3CA-related disorders (PROS) in humans

Activating *PIK3CA* mutations have been associated with many human overgrowth disorders categorized based on severity and distribution of the mutation. Involvement of multiple tissues results in CLOVES or Klippel-Trenaunay syndrome with highly mosaic mutation levels (0.8-32%) in affected tissues[37,38]. Involvement of single tissue or body segment results in epidermal nevi, lymphatic malformations or other localized phenotypes with usually no mutations detected in unaffected tissues[7,37-44]. Too few patients and insufficient quantitative data have been reported to observe allele-specific differences.

In the brain, mosaic hotspot mutations result in SEGCD, classified as dysplastic MEG, HMEG or FCD2a based on extent of lesion[27]. *PIK3CA* mutations were detected in 9/73 patients with HMEG and 1/33 with FCD2[8,9,27]. These overlapping SEGCD are associated with severe and usually intractable epilepsy[14-16,45-49]. ~20 other *PIK3CA* mutant alleles have been seen in MCAP, characterized by MEG or MEG-PMG, hydrocephalus and less severe epilepsy[6,12,13,50].

We activated the two most common hotspot mutations, *E545K* and *H1047R*, in mouse brain at different developmental timepoints to generate the first models of human *PIK3CA*-related SEGCD. Our mouse models faithfully recapitulated the most important *PIK3CA*-related phenotypes of MEG, hydrocephalus, cortical and white matter dysplasia, and epilepsy (**Table 1**).

Differential activating mechanisms underlie *Pik3ca* allele-specific brain phenotypes

Data from cancer biology suggests that *H1047* mutation is more severe than *E545K* mutation. For example, *E545K* mutation accounts for 1932/7548 (26%) and *H1047R* for 2898/7548 (38%) of *PIK3CA*-coding mutations detected in the COSMIC database of cancer mutations (http://cancer.sanger.ac.uk/cancergenome/projects/cosmic/).

We found that *H1047R* and *E545K* mutations caused distinct phenotypes in mice, *H1047R* being more severe than *E545K*. *hGFAP-cre;H1047R* mutants had severe hydrocephalus and died pre-weaning. In contrast all mice with the *E545K* allele survived through adulthood without hydrocephalus. Developmental analyses of *hGFAP-cre;H1047R* and *Nestin-cre;E545K* embryos revealed common mechanisms, such as larger neurons and lower cell densities, contributing to enlarged brain size, with differences more significant in *H1047R* mutants. *E545K* mutation also elevated cortical proliferation and cell cycle exit during late neurogenesis. We do not believe that overexpression of the transgenic *H1047R* allele versus the knock-in design of the *E545K* allele underlies the phenotypic differences. The PI3K enzyme is made of p110 (encoded by *Pik3ca*) and p85 subunits. p110 stability is entirely dependent on levels of p85[51-53] and we have not altered p85. Rather, the phenotypic differences more likely reflect distinct allele-specific overactivation of PI3K signaling. The *H1047R* mutation increases the level and duration of response to extracellular ligand, while *E545K* alters the helical domain resulting in constitutive low level signaling with a blunted response to extracellular ligands[54,55].

These differences likely reflect distinct mechanisms differentially altering PI3K signaling. Whereas *H1047R* mutation increases the level and duration of response to extracellular ligand, *E545K* alters the helical domain resulting in constitutive low level signaling with a blunted response to extracellular ligands[54,55].

Effect of *Pik3ca* overactivation on brain and cell size is temporally regulated

By activating the *E545K* mutation in progressively limited progenitor pools, we decreased the size of brain and cells in a graduated fashion. Postnatal *E545K* activation had no impact on cell/brain size. We conclude that the *PIK3CA*-related brain overgrowth must arise from mosaic mutations in embryonic neural progenitors.

Although neuronal size was enlarged in both *hGFAP-cre;H1047R* and *Nestin-cre;E545K* mutants, it was less than that observed in *Pten null* mice or in cultured hippocampal neurons constitutively overexpressing *Akt*[56,57]. Multiple models of *Pten* deletion cause progressive increases in postnatal neuronal size and increased brain size without continued proliferation[57-60]. Our *Nestin-cre;E545K* mutants had enlarged brain size evident at birth, without progressive increases in postnatal cell size. This is congruent with the analysis of resected human brain tissue from SEGCD patients. Mild cellular enlargement was observed with *PIK3CA* mutations in contrast to marked enlargement with *PTEN* or *AKT3* mutations[27].

Aberrant neuronal migration is a major contributor to Pik3ca-related cortical dysplasia

Brains of SEGCD patients show mild to moderate migration defects in early-born cortical neurons and more severe defects in late-born neurons[23,24]. Similarly, embryonic

activation of *H1047R* and *E545K* in mice caused abnormal neocortical lamination, with late-migrating Cux1-positive neurons severely affected in both the mutants. Birthdating studies support the conclusion that Pik3ca activation does not alter cell fate and that cortical dysplasia is predominantly a result of aberrant migration. The severity of dyslamination in *H1047R* mutants likely reflects the dysplastic Reelin-positive Cajal-Retzius cells. However the Reelin-positive layer remained well defined in both mutants. This is in contrast to the ectopic Reelin expression in neurons expressing high levels of overactive pAKT introduced by electroporation into embryonic mouse cortex[61]. In human SEGCD, late migrating neurons often fail to migrate to the upper layers[23], a phenotype more severe than seen in any of our mouse models. However, NeuN immunohistochemistry in *H1047R* mutants confirmed the presence of ectopic neurons in the subcortical white matter, as seen in human SEGCD brain[23,62]. Human MEG is associated with a wide range of white matter dysplasia ranging from agenesis of corpus callosum to thickening of subcortical axon bundles[10,25-27,62]. These features were also faithfully recapitulated in our mouse models.

Pik3ca-related epilepsy is an active Pik3ca-dependent process dissociable from dysmorphology

Both adult megalencephaic *Nestin-cre;E545K* and normocephalic *Nestin-creER;E545K* mice exhibited spontaneous seizures as well as lowered seizure thresholds upon PTZ-seizure induction. Although cortical dysplasia resulted from embryonic activation of *Pik3ca* in *Nestin-cre;E545K* mice, postnatal activation of *Nestin-creER;E545K* did not cause increased cell size or megalencephaly or altered cortical

lamination. Thus Pik3ca-dependent epilepsy is independent of dysmorphology. Further, inhibitory interneurons were not grossly perturbed in *Nestin-creER;E545K* mice (data not shown). This is congruent with the fact that these interneurons are born at embryonic stages and their migration is almost complete before birth[63]. Therefore, although altered interneuron development in *Nestin-cre;E545K* may contribute to epilepsy, aberrant interneuron development cannot represent a common mechanism for epilepsy in both models. The observation that acute BKM120 treatment is sufficient to inhibit PTZ-induced seizures even in adult megalencephalic mice supports the argument that the epileptic seizures are independent of dysplasia since the latter is not reversed over the short course of treatment. This is an important finding since a large portion of FCD patients who do not show detectable dysplasia suffer from intractable epilepsy[64].

Proteomic analyses of cell signaling networks in megalencephalic cortical and hippocampal tissue at baseline and treated with PTZ and/or BKM120 provide insight into the mechanism of Pik3ca-dependent epilepsy. *Nestin-cre;E545K* mutants had elevated PI3K signaling with a more robust upregulation of mTOR-dependent pS473-Akt than the direct PDK1-dependent pT308-Akt, similar to recent findings in PIK3CA human brain samples[27]. The modest changes in signaling compared to controls is congruent with previous studies which demonstrated only modest changes in the steady-state levels of PI3K signaling in breast cancer cells with *PIK3CA* mutations[65]. Higher signaling levels in hippocampus versus cortex suggest a more prominent role of hippocampus in the seizure phenotype. PTZ administration alone in both controls and megalencephalic *Nestin-cre;E545K* mutants caused upregulation of many core

components of PI3K-AKT pathway, including pAkt, pS6 and pNDRG1. This is congruent with a report showing PTZ-induced seizures in rats upregulated PI3K-AKT-mTOR pathway[66] and suggests that elevated baseline PI3K signaling levels are epileptogenic.

Indeed, there is extensive human and mouse evidence that elevated mTOR signaling is epileptogenic although the mechanisms for the epilepsy are incompletely understood. A number of mechanisms including altered development, cell size, growth, proliferation and circuitry have been reported[67]. Most remarkably however, our acute BKM120 administration data clearly demonstrates that histopathological mechanisms are not the primary epilepsy drivers. Acute, one hour of BKM120 administration was sufficient to completely inhibit the increased phosphorylation levels induced by PTZ, notably returning mutant hippocampal mTOR-dependent pS473-AKT levels to baseline untreated control levels. This was sufficient to normalize the PTZ-seizure induction threshold, despite continued dysplasia in *Nestin-cre;E545K* mutants. We conclude that elevated PI3K signaling is itself actively epileptogenic, independent of underlying developmental pathology.

Changing the face of intractable pediatric epilepsy

The discovery that *Pik3ca*-related epilepsy is independent of dysplasia and susceptible to acute modulation is a major and paradigm shifting finding. Since PIK3CA resides at the top of the PI3K-AKT pathway, our mouse models represent surrogates for the entire group of patients with segmental brain overgrowth, including patients with somatic mosaic mTOR and AKT3 mutations[7-12]. SEGCD is associated with early onset, severe and frequently intractable epilepsy that responds poorly to standard seizure medications[14-16,45-47]. Epilepsy surgery has been comparatively more successful (73%)

437 in combating seizures in the same children[15]. A drug-based therapy however, would
438 clearly be preferable. mTOR inhibition with rapamycin has shown therapeutic promise in
439 FCD patients and animals models[61,68-70]; however, rapamycin treatments are not acute.
440 Our data demonstrates that acute small molecule-based modulation of PI3K signaling,
441 despite the presence of dysplasia, has dramatic therapeutic benefit. This suggests that
442 PI3K inhibitors offer a promising new avenue for effective antiepileptic therapy for large
443 cohorts intractable pediatric epilepsy patients.

MATERIALS and METHODS

Mice

The following mouse lines were used: *Nestin-cre* (Jackson Labs, Stock #003771), *Nestin-creERT2* lines (Jackson Labs, MGI:3641212 and line generated in SJB's lab, Zhu et al., 2012), human glial fibrillary acidic protein (*hGFAP*)-cre (Jackson Labs, Stock #004600), *Pik3ca*^{H1047R} transgenic (human *H1047R* transgene expression is under the control of a tetracycline-inducible promoter (TetO))[18], *Rosa26-rtTA* line (Jackson Labs, Stock #005670), *Pik3ca*^{E545K} knock-in[20], Ai-9 (Jackson Labs, Stock #007905), Ai-14 (Jackson Labs, Stock # 007914), *R26-LSL-EYFP* (Jackson Labs, Stock #006148), *Rosa26-LacZ* (Jackson Labs # 003474). We have designated the *Pik3ca*^{H1047R} and *Pik3ca*^{E545K} conditional mutant mice as *H1047R* and *E545K* mutants/lines throughout the manuscript.

All lines were maintained on a mixed genetic background, comprising of FVB, C57Bl6, 129 and CD1 strains. Noon of the day of vaginal plug was designated as embryonic day 0.5 (E0.5). The day of birth was designated as postnatal day 0 (P0). The *H1047R* and *Rosa26-rtTA* lines were intercrossed and female mice positive for both these alleles were crossed with *hGFAP-cre;RosartTA;Pik3ca*^{H1047R} males. To ensure that *cre* and *Pik3ca*^{H1047R} mutant transgene expression was correlated plugged females were treated with doxycycline (Sigma; 2mg/ml) from E0.5 available *ad libitum* in drinking water. For the neonatal induction experiment, the pups were treated with doxycycline from P1. The *E545K* line was crossed to reporter lines to obtain *E545K* floxed allele and the reporter in the same mouse line. Tamoxifen (Sigma T5648) was dissolved at 37^{o}C in

corn oil (Sigma) at 5mg/ml and was administered intraperitoneally to pups of the cross *Nestin-creER* X *Pik3ca*^{E545K} mice at a dose of 75µg/g body weight, once a day at P0 and P1, to activate the *E545K* mutation postnatally. *hGFAP–cre, Nestin–cre* and *Nestin–creERT2* mice were genotyped by PCR using primers for the *cre* coding region, as previously described[71]. Genotyping of other alleles were done according to the following references: *H1047R* and *Rosa+/-*[18], *E545Kfloxed/+*[20], *EYFP/+* and *Ai9/+* [72]. All mouse procedures were approved by the Institutional Animal Care and Use Committees.

Sample preparation and histochemical procedures

Embryos and postnatal pups were harvested in phosphate buffer saline (PBS); brains fixed in 4% paraformaldehyde (PFA) for 4 hours, equilibrated in 30% (wt/vol) sucrose made in PBS, and sectioned at 25µm on a freezing microtome. Adult mice were perfused with 4%PFA, brains collected and fixed in 4%PFA overnight, sunk in 30% sucrose in PBS, embedded in optimum cutting temperature (OCT) compound and sectioned at 12µm on a cryostat. Sections were then processed for Nissl, hematoxylin and eosin (H&E) or immunohistochemical staining.

Immunohistochemistry: Sections were washed thrice in PBS, boiled in 10mM Sodium citrate solution for antigen retrieval, blocked in 5% serum in PBS with 0.1%Triton X-100 and then incubated overnight at 4°C with primary antibodies. The next day, sections were washed thrice in PBS, incubated with appropriate species-specific secondary antibodies conjugated with Alexa 488, 568, 594 or 647 fluorophores (Invitrogen) for 2 h at room temperature and then counterstained with DAPI to visualize nuclei. Sections were coverslipped using Fluorogel (EMS #17985) mounting medium. Immunostained

sections were imaged in Zeiss LSM 710 Imager Z2 laser scanning confocal microscope using Zen 2009 software and later processed in ImageJ software (NIH, Bethesda, Maryland, USA). Primary antibodies used are: rat anti-BrdU (Abcam), mouse anti-BrdU (Roche), rabbit anti-Tbr1(EMD Millipore), mouse anti-Tbr2 (EMD Millipore), rat anti-Ctip2 (Abcam), rabbit anti-Cux1/CDP (Santa Cruz Biotechnology), rabbit anti-pS6 (Cell Signaling), mouse anti-NeuN (EMD Millipore), mouse anti-Reelin (EMD Millipore), rabbit anti-Laminin (Sigma), rabbit anti-Olig2 (EMD Millipore), mouse anti-Nestin (EMD Millipore), chicken anti-YFP (Abcam), rabbit anti-Ki67 (Vector Lab), mouse anti-S100 (Abcam).

Nissl and H&E staining: Sections were stained in 0.1% cresyl violet solution for 10min, rinsed quickly in distilled water, dehydrated in 95% ethanol, and left in xylene before being coverslipped with Permount (Fischer Scientific). H&E staining was performed by passing the sections through Harris modified Hematoxylin solution (Fisher Scientific) and EosinY (Sigma) and then dehydrating them in increasing grades of ethanol before dipping in xylene and coverslipping. Brightfield images were taken in Leica MZFLIII microscope using Leica DFC425 camera and LAS V3.8 software.

BrdU Incorporation Experiments

Bromodeoxyuridine (BrdU; Life Technologies) was administered intraperitoneally (100 µg/g of body weight) to pregnant mice at E14.5/16.5 for 1 hour, at E15.5 for 1 day and at E12.5/E16.5 for proliferation assays, cell cycle exit and birthdating experiments respectively. S-phase labeling index (LI) was calculated by dividing total $BrdU^+$ cells by

total number of $DAPI^+$ cells. Quit fraction was calculated by dividing $BrdU^+Ki67^-$ cells by total number of $BrdU^+$ cells.

β-Gal staining protocol

Brain sections were briefly fixed, washed in wash buffer at room temperature and then stained overnight at 37°C in the staining solution comprising of the X-gal substrate. The sections were then washed in wash buffer at room temperature and stored at 4°C.

TUNEL staining

TUNEL staining was processed on E16.5 control and mutant sections using Roche In situ Cell Death Detection Kit, Fluorescein.

Magnetic Resonance Imaging (MRI) for volumetric analysis

At least 5 mice of each genotype (age P40-60) were used for volumetric analyses. MRI study was performed using a 7 T Bruker ClinScan system (Bruker BioSpin MRI GmbH, Germany) equipped with 12S gradient coil. A 2-channel surface coil was used for MR imaging. Animals were anesthetized and maintained with 1.5% isoflurane during MRI sessions. Transverse T2-weighted turbo spin echo images were acquired for volume measurements (TR/TE = 3660/50 ms, FOV = 25 x25mm, matrix = 320x320, NEX = 1, Thickness = 0.4 mm, scan time = 6.5 min). Total brain volumes were obtained by manually segmenting brain regions from olfactory bulbs to cerebellum, and computing volumes using OsiriX (Pixmeo, Switzerland). Each data point in the graph represents 1 mouse.

Seizure experiments

Mice obtained from the following crosses were used for experiments at ~P35 (young age) and ~P180 (old age): *Nestin-cre*/+ X *Pik3ca*^{E545K}*floxed*/+ and *Nestin-creER*/+ X *Pik3ca*^{E545K}*floxed*/+. At least 5 animals of each genotype were used per treatment experiment.

Pentylenetetrazole (PTZ) seizure test. Mice were subcutaneously injected with PTZ (Sigma), a GABA (A) receptor-antagonist, at 40mg/kg body weight and digital videos of the mice were recorded for 30mins post-PTZ injection. Principal behavior in each 10 second-bin of the recorded video was scored as 4 or 5 using the Racine scale of seizure severity (4, rearing with forelimb clonus; and 5, rearing and falling with forelimb clonus)[73,74]. *Treatment trials.* Pan-PI3K inhibitor BKM-120 (Novartis; 50mg/kg body weight, dissolved in 0.5% Tween-80, 0.5% methylcellulose) or saline was administered by oral gavage to the mice 1hr before PTZ seizure test.

Sleep deprivation (SD). To permit control of circadian variations of sleep in these experiments, baseline (control) sleep data (Pre SD) were recorded from mice one day before they were submitted to total sleep deprivation. Mice were allowed to sleep normally for 5 continuous hours beginning at 8:00 AM, and then baseline sleep video-EEG recordings were obtained continuously in the 1 subsequent hour. On the following day, beginning at 8:00 AM, the same mice were kept awake for 5 consecutive hours by random gentle touches with a rotating light curtain attached to a motor mounted on the lid of the sleep deprivation chamber. The motor was in turn, connected to a computer via Power Lab (ADInstruments, Colorado Spring, CO). The random direction and speed

559 of the motor rotation were custom-programmed in the stimulator panel dialog box of
560 LabChart 8 Software (ADInstruments, Colorado Spring, CO). The specific parameters
561 used are tabulated as **Supplementary file 1**. Post sleep deprivation, mice were not
562 disturbed and post SD recordings were obtained for 2h.

563 *Video-electroencephalagraphy-electromyography (Video-EEG-EMG) recording.* These
564 experiments were performed as previously described[73] . Briefly, mice underwent
565 survival surgery to implant fine (diameter: 130μm bare; 180μm coated) silver wire EEG
566 and EMG electrodes under isoflurane anesthesia. Four EEG electrodes were placed
567 bilaterally through the small cranial burr holes over the posterior and frontal cortices and
568 were fixed in place with cyanoacrylate glue and dental cement (Lang Dental
569 Manufacturing Co., Inc., Wheeling, IL). Similarly, one reference electrode was placed
570 above the cerebellum. A ground electrode was inserted subcutaneously over the back.
571 EMG electrodes were placed in back muscles. Only 2 electrodes were implanted in the
572 young *Nestin-cre;E545K* mutant and control mice. Mice were allowed to recover from
573 surgery for 2-3 days. Simultaneous video-EEG-EMG recordings were collected from
574 conscious mice on a PowerLab 8/35 data acquisition unit using LabChart 7.3.3 software
575 (AD Instruments, Colorado Spring, Co). All bioelectrical signals were acquired at 1KHz
576 sampling rate. The EEG signals were processed off-line with a 1-70 Hz bandpass filter
577 and the ECG signals with a 3-Hz highpass filter. Interictal spikes were identified as
578 transient, clearly distinguished from background activity, with pointed peak and short
579 duration. Myoclonic seizures were identified as shock-like jerks of the muscles on video
580 associated with a spike or polyspike-wave complex on EEG.

581

Reverse Phase Protein Array (RPPA) Analysis

Cortex and hippocampus were dissected out of P35 control and *E545K* mutant mice, following different treatments (vehicle only (-), +BKM120, +PTZ, +BKM120+PTZ), and flash-frozen in liquid nitrogen then sent to the RPPA Core Facility at MD Anderson Cancer Center, University of Texas. Three independent biological replicates per sample were analyzed. Analysis was performed as previously described[36]. The mouse brain tissue samples were lysed and underwent protein extraction. Cellular protein was denatured by SDS sample buffer and serial dilution was made for each sample. Cell lysates were then probed with different validated antibodies. Signals were detected by DAB colorimetric reaction and intensity was quantified using ArrayPro software. Protein concentration was determined by super curve fitting. All the data points were normalized for protein loading and transformed to linear value. These linear values were used to make bar graphs for comparative analysis. See *http://www.mdanderson.org/education-and-research/resources-for-professionals/scientific-resources/core-facilities-and-services/functional-proteomics-rppa-core/index.html*) for a detailed antibody list and protocols.

Quantitative Analysis

For quantitative analysis of embryos, data was collected from comparable sections of a minimum of 3 embryos of each genotype (from 2 or more independent litters) at each developmental stage. Cortical length was measured in the lateral ventricular lining from the tip of the fimbria/cortical hem to the pallial-subpallial boundary. Cortical length and thickness were measured using ImageJ software (NIH, Bethesda, Maryland, USA); the data was normalized to the control value. Cell counts from E14.5 and E16.5 brains were

606 obtained from 25% of the neocortex. Area of interest was derived by dividing the whole
607 length of neocortex into quarters and then taking images of the total area, from pia to
608 ventricle, in the third quartile from dorsal midline. Confocal stacks of immunostained
609 sections of each developmental stage were generated by scanning at intervals of
610 0.99μm using filters of appropriate wavelengths at 20X and 40X magnifications.
611 Confocal images of DAPI-stained brain sections and NeuN/pS6-immunostained
612 sections were used to measure nuclear and cell size respectively. Measurements for
613 labeling index, quit fraction, birthdating studies, cell density and size were calculated
614 using ImageJ. For zonal quantification of cells, the cortical column was divided into 5
615 different parts – the ventricular-subventricular zone (vz/svz), white matter, and 3 equally
616 divided zones of the neocortical plate (lower, mid, upper).
617
618 Statistical significance was assessed using 2-tailed unpaired t-tests (for cortical length
619 and thickness, cell density, nuclear size, TUNEL assay, labeling index, quit fraction,
620 total cell counts and seizure data) and ANOVA followed by Bonferroni (for cell size,
621 BKM treatment data, birthdating experiments) and Tukey (for RPPA graphs) post-tests.
622 These analyses were performed in GraphPad Prism v5.01 (GraphPad Software Inc.,
623 San Diego, USA) or in Igor Pro v6.3.6.4, Igor Pro Software, Lake Oswego, USA.
624 Differences were considered significant at $P < 0.05$.

ACKNOWLEDGMENT

We thank Leon Murphy (Novartis) for BKM120, Taylor Faubion for technical support, Joseph Gleeson for sharing unpublished data and Ghayda Mirzaa and Laura Jansen for discussions.

REFERENCES

1. Cheung, M. & Testa, J.R. Diverse mechanisms of AKT pathway activation in human malignancy. *Curr Cancer Drug Targets* **13**, 234-244 (2013).
2. Engelman, J.A. Targeting PI3K signalling in cancer: opportunities, challenges and limitations. *Nat Rev Cancer* **9**, 550-562 (2009).
3. Hennessy, B.T., Smith, D.L., Ram, P.T., Lu, Y. & Mills, G.B. Exploiting the PI3K/AKT pathway for cancer drug discovery. *Nat Rev Drug Discov* **4**, 988-1004 (2005).
4. Iwabuchi, H.*, et al.* Genetic analysis of benign, low-grade, and high-grade ovarian tumors. *Cancer Res* **55**, 6172-6180 (1995).
5. Samuels, Y. & Waldman, T. Oncogenic mutations of PIK3CA in human cancers. *Curr Top Microbiol Immunol* **347**, 21-41 (2010).
6. Gymnopoulos, M., Elsliger, M.A. & Vogt, P.K. Rare cancer-specific mutations in PIK3CA show gain of function. *Proc Natl Acad Sci U S A* **104**, 5569-5574 (2007).
7. Keppler-Noreuil, K.M.*, et al.* Clinical delineation and natural history of the PIK3CA-related overgrowth spectrum. *Am J Med Genet A* **164A**, 1713-1733 (2014).
8. Lee, J.H.*, et al.* De novo somatic mutations in components of the PI3K-AKT3-mTOR pathway cause hemimegalencephaly. *Nat Genet* **44**, 941-945 (2012).
9. D'Gama, A.M.*, et al.* mTOR pathway mutations cause hemimegalencephaly and focal cortical dysplasia. *Ann Neurol* (2015).
10. Conway, R.L.*, et al.* Neuroimaging findings in macrocephaly-capillary malformation: a longitudinal study of 17 patients. *Am J Med Genet A* **143A**, 2981-3008 (2007).
11. Jansen, L.A.*, et al.* PI3K/AKT pathway mutations cause a spectrum of brain malformations from megalencephaly to focal cortical dysplasia. *Brain* **138**, 1613-1628 (2015).
12. Mirzaa, G.M.*, et al.* Megalencephaly-capillary malformation (MCAP) and megalencephaly-polydactyly-polymicrogyria-hydrocephalus (MPPH) syndromes: two closely related disorders of brain overgrowth and abnormal brain and body morphogenesis. *Am J Med Genet A* **158A**, 269-291 (2012).
13. Riviere, J.B.*, et al.* De novo germline and postzygotic mutations in AKT3, PIK3R2 and PIK3CA cause a spectrum of related megalencephaly syndromes. *Nat Genet* **44**, 934-940 (2012).
14. Bast, T., Ramantani, G., Seitz, A. & Rating, D. Focal cortical dysplasia: prevalence, clinical presentation and epilepsy in children and adults. *Acta neurologica Scandinavica* **113**, 72-81 (2006).
15. Fauser, S.*, et al.* Long-term seizure outcome in 211 patients with focal cortical dysplasia. *Epilepsia* **56**, 66-76 (2015).
16. Fauser, S.*, et al.* Clinical characteristics in focal cortical dysplasia: a retrospective evaluation in a series of 120 patients. *Brain* **129**, 1907-1916 (2006).
17. Kinross, K.M.*, et al.* An activating Pik3ca mutation coupled with Pten loss is sufficient to initiate ovarian tumorigenesis in mice. *J Clin Invest* **122**, 553-557 (2012).
18. Liu, P.*, et al.* Oncogenic PIK3CA-driven mammary tumors frequently recur via PI3K pathway-dependent and PI3K pathway-independent mechanisms. *Nat Med* **17**, 1116-1120 (2011).
19. Meyer, D.S.*, et al.* Luminal expression of PIK3CA mutant H1047R in the mammary gland induces heterogeneous tumors. *Cancer Res* **71**, 4344-4351 (2011).
20. Robinson, G.*, et al.* Novel mutations target distinct subgroups of medulloblastoma. *Nature* **488**, 43-48 (2012).
21. Yuan, W.*, et al.* Conditional activation of Pik3ca(H1047R) in a knock-in mouse model promotes mammary tumorigenesis and emergence of mutations. *Oncogene* **32**, 318-326 (2013).

22. Maira, S.M.*, et al.* Identification and characterization of NVP-BKM120, an orally available pan-class I PI3-kinase inhibitor. *Mol Cancer Ther* **11**, 317-328 (2012).
23. Arai, A.*, et al.* Abnormal maturation and differentiation of neocortical neurons in epileptogenic cortical malformation: unique distribution of layer-specific marker cells of focal cortical dysplasia and hemimegalencephaly. *Brain Res* **1470**, 89-97 (2012).
24. Rossini, L.*, et al.* Layer-specific gene expression in epileptogenic type II focal cortical dysplasia: normal-looking neurons reveal the presence of a hidden laminar organization. *Acta Neuropathol Commun* **2**, 45 (2014).
25. Adamsbaum, C.*, et al.* Focal cortical dysplasia and hemimegalencephaly: histological and neuroimaging correlations. *Pediatr Radiol* **28**, 583-590 (1998).
26. De Rosa, M.J., Secor, D.L., Barsom, M., Fisher, R.S. & Vinters, H.V. Neuropathologic findings in surgically treated hemimegalencephaly: immunohistochemical, morphometric, and ultrastructural study. *Acta Neuropathol* **84**, 250-260 (1992).
27. Jansen, L.A.*, et al.* PI3K/AKT pathway mutations cause a spectrum of brain malformations from megalencephaly to focal cortical dysplasia. *Brain* **in press**(2015).
28. Sosunov, A.A.*, et al.* Tuberous sclerosis: a primary pathology of astrocytes? *Epilepsia* **49 Suppl 2**, 53-62 (2008).
29. Zeng, L.H., Xu, L., Gutmann, D.H. & Wong, M. Rapamycin prevents epilepsy in a mouse model of tuberous sclerosis complex. *Ann Neurol* **63**, 444-453 (2008).
30. Giorgi, F.S.*, et al.* Controversial issues on EEG after sleep deprivation for the diagnosis of epilepsy. *Epilepsy Res Treat* **2013**, 614685 (2013).
31. Binnie, C.D. & Prior, P.F. Electroencephalography. *J Neurol Neurosurg Psychiatry* **57**, 1308-1319 (1994).
32. Kalume, F.*, et al.* Sleep impairment and reduced interneuron excitability in a mouse model of Dravet Syndrome. *Neurobiol Dis* **77**, 141-154 (2015).
33. Macdonald, R.L. & Barker, J.L. Specific antagonism of GABA-mediated postsynaptic inhibition in cultured mammalian spinal cord neurons: a common mode of convulsant action. *Neurology* **28**, 325-330 (1978).
34. Bendell, J.C.*, et al.* Phase I, dose-escalation study of BKM120, an oral pan-Class I PI3K inhibitor, in patients with advanced solid tumors. *J Clin Oncol* **30**, 282-290 (2012).
35. Brachmann, S.M.*, et al.* Characterization of the mechanism of action of the pan class I PI3K inhibitor NVP-BKM120 across a broad range of concentrations. *Mol Cancer Ther* **11**, 1747-1757 (2012).
36. Tibes, R.*, et al.* Reverse phase protein array: validation of a novel proteomic technology and utility for analysis of primary leukemia specimens and hematopoietic stem cells. *Mol Cancer Ther* **5**, 2512-2521 (2006).
37. Luks, V.L.*, et al.* Lymphatic and other vascular malformative/overgrowth disorders are caused by somatic mutations in PIK3CA. *J Pediatr* **166**, 1048-1054 e1041-1045 (2015).
38. Kurek, K.C.*, et al.* Somatic mosaic activating mutations in PIK3CA cause CLOVES syndrome. *Am J Hum Genet* **90**, 1108-1115 (2012).
39. Osborn, A.J.*, et al.* Activating PIK3CA alleles and lymphangiogenic phenotype of lymphatic endothelial cells isolated from lymphatic malformations. *Hum Mol Genet* **24**, 926-938 (2015).
40. Groesser, L., Herschberger, E., Landthaler, M. & Hafner, C. FGFR3, PIK3CA and RAS mutations in benign lichenoid keratosis. *Br J Dermatol* **166**, 784-788 (2012).
41. Lindhurst, M.J.*, et al.* Mosaic overgrowth with fibroadipose hyperplasia is caused by somatic activating mutations in PIK3CA. *Nat Genet* **44**, 928-933 (2012).
42. Hafner, C.*, et al.* Oncogenic PIK3CA mutations occur in epidermal nevi and seborrheic keratoses with a characteristic mutation pattern. *Proc Natl Acad Sci U S A* **104**, 13450-13454 (2007).

43. Rios, J.J., *et al.* Somatic gain-of-function mutations in PIK3CA in patients with macrodactyly. *Hum Mol Genet* **22**, 444-451 (2013).
44. Cohen, A.S., *et al.* Somatic mosaicism for the p.His1047Arg mutation in PIK3CA in a girl with mesenteric lipomatosis. *Am J Med Genet A* **164A**, 2360-2364 (2014).
45. Pasquier, B., *et al.* Surgical pathology of drug-resistant partial epilepsy. A 10-year-experience with a series of 327 consecutive resections. *Epileptic Disord* **4**, 99-119 (2002).
46. Russo, G.L., *et al.* Focal cortical resection in malformations of cortical development. *Epileptic Disord* **5 Suppl 2**, S115-123 (2003).
47. Tassi, L., *et al.* Focal cortical dysplasia: neuropathological subtypes, EEG, neuroimaging and surgical outcome. *Brain* **125**, 1719-1732 (2002).
48. Devlin, A.M., *et al.* Clinical outcomes of hemispherectomy for epilepsy in childhood and adolescence. *Brain* **126**, 556-566 (2003).
49. Blumcke, I., *et al.* The clinicopathologic spectrum of focal cortical dysplasias: a consensus classification proposed by an ad hoc Task Force of the ILAE Diagnostic Methods Commission. *Epilepsia* **52**, 158-174 (2011).
50. Mirzaa, G.M., Riviere, J.B. & Dobyns, W.B. Megalencephaly syndromes and activating mutations in the PI3K-AKT pathway: MPPH and MCAP. *Am J Med Genet C Semin Med Genet* **163**, 122-130 (2013).
51. Geering, B., Cutillas, P.R., Nock, G., Gharbi, S.I. & Vanhaesebroeck, B. Class IA phosphoinositide 3-kinases are obligate p85-p110 heterodimers. *Proc Natl Acad Sci U S A* **104**, 7809-7814 (2007).
52. Fruman, D.A., *et al.* Hypoglycaemia, liver necrosis and perinatal death in mice lacking all isoforms of phosphoinositide 3-kinase p85 alpha. *Nat Genet* **26**, 379-382 (2000).
53. Yu, J., *et al.* Regulation of the p85/p110 phosphatidylinositol 3'-kinase: stabilization and inhibition of the p110alpha catalytic subunit by the p85 regulatory subunit. *Mol Cell Biol* **18**, 1379-1387 (1998).
54. Miled, N., *et al.* Mechanism of two classes of cancer mutations in the phosphoinositide 3-kinase catalytic subunit. *Science* **317**, 239-242 (2007).
55. Zhao, L. & Vogt, P.K. Helical domain and kinase domain mutations in p110alpha of phosphatidylinositol 3-kinase induce gain of function by different mechanisms. *Proc Natl Acad Sci U S A* **105**, 2652-2657 (2008).
56. Kumar, V., Zhang, M.X., Swank, M.W., Kunz, J. & Wu, G.Y. Regulation of dendritic morphogenesis by Ras-PI3K-Akt-mTOR and Ras-MAPK signaling pathways. *J Neurosci* **25**, 11288-11299 (2005).
57. Kwon, C.H., *et al.* Pten regulates neuronal soma size: a mouse model of Lhermitte-Duclos disease. *Nat Genet* **29**, 404-411 (2001).
58. Fraser, M.M., *et al.* Pten loss causes hypertrophy and increased proliferation of astrocytes in vivo. *Cancer Res* **64**, 7773-7779 (2004).
59. Fraser, M.M., Bayazitov, I.T., Zakharenko, S.S. & Baker, S.J. Phosphatase and tensin homolog, deleted on chromosome 10 deficiency in brain causes defects in synaptic structure, transmission and plasticity, and myelination abnormalities. *Neuroscience* **151**, 476-488 (2008).
60. Backman, S.A., *et al.* Deletion of Pten in mouse brain causes seizures, ataxia and defects in soma size resembling Lhermitte-Duclos disease. *Nat Genet* **29**, 396-403 (2001).
61. Baek, S.T. An AKT3-FOXG1-Reelin Network Underlies Human Focal Malfomrations of Cortical Development. *Nat Med* (2015).
62. Salamon, N., *et al.* Contralateral hemimicrencephaly and clinical-pathological correlations in children with hemimegalencephaly. *Brain* **129**, 352-365 (2006).

63. Batista-Brito, R. & Fishell, G. The developmental integration of cortical interneurons into a functional network. *Curr Top Dev Biol* **87**, 81-118 (2009).
64. Bernasconi, A., Bernasconi, N., Bernhardt, B.C. & Schrader, D. Advances in MRI for 'cryptogenic' epilepsies. *Nat Rev Neurol* **7**, 99-108 (2011).
65. Stemke-Hale, K.*, et al.* An integrative genomic and proteomic analysis of PIK3CA, PTEN, and AKT mutations in breast cancer. *Cancer Res* **68**, 6084-6091 (2008).
66. Zhang, B. & Wong, M. Pentylenetetrazole-induced seizures cause acute, but not chronic, mTOR pathway activation in rat. *Epilepsia* **53**, 506-511 (2012).
67. Wong, M. & Crino, P.B. mTOR and Epileptogenesis in Developmental Brain Malformations. (2012).
68. Curatolo, P. & Moavero, R. mTOR inhibitors as a new therapeutic option for epilepsy. *Expert Rev Neurother* **13**, 627-638 (2013).
69. Lim, J.S.*, et al.* Brain somatic mutations in MTOR cause focal cortical dysplasia type II leading to intractable epilepsy. *Nat Med* **21**, 395-400 (2015).
70. Moon, U.Y.*, et al.* Impaired Reelin-Dab1 Signaling Contributes to Neuronal Migration Deficits of Tuberous Sclerosis Complex. *Cell Rep* **12**, 965-978 (2015).
71. Chizhikov, V.V.*, et al.* The roof plate regulates cerebellar cell-type specification and proliferation. *Development* **133**, 2793-2804 (2006).
72. Zhu, G.*, et al.* Pten deletion causes mTorc1-dependent ectopic neuroblast differentiation without causing uniform migration defects. *Development* **139**, 3422-3431 (2012).
73. Kalume, F. Sudden unexpected death in Dravet syndrome: respiratory and other physiological dysfunctions. *Respir Physiol Neurobiol* **189**, 324-328 (2013).
74. Racine, R.J. Modification of seizure activity by electrical stimulation. II. Motor seizure. *Electroencephalogr Clin Neurophysiol* **32**, 281-294 (1972).

FIGURE LEGENDS

Figure1: Embryonic *Pik3ca* overactivation in mice causes MEG

(a,b) Compared to control, P21 *hGFAP-cre;H1047R* mutants had domed foreheads. (c,d) Coronal section of H&E-stained P3 *H1047R* mutant showed bigger brain and enlarged lateral ventricles compared to control. Mutant neocortex (nctx) was dysplastic and medial tissue highly infolded (arrowhead; d). (e-g) P35 *hGFAP-cre;E545K* and *Nestin-cre;E545K* brains were noticeably larger than controls, while *Nestin-creER*;*E545K* mutants had normal-sized brains compared to controls. Red color of *Nestin-creER;E545K* brain is due to presence of a lox-stop-lox-Tomato reporter allele, and shows successful induction of cre activity. Controls for e,f and g are of genotypes *Pik3ca E545K, hGFAP-cre, Nestin-cre* and *Nestin-creER.* (h) MRI volumetric analyses of mutant and corresponding control brains. *, $p<0.0001$; ns, not significant. Each data point in the graph represents 1 mouse. (i-l) Nissl-stained coronal sections of representative control and mutant brains. Scale bars: 1mm (c,d); 2mm (i-l). See also Figure 1 – figure supplements 1-3.

Figure2: *Pik3ca* activating mutations lead to increased embryonic cortical length

(a) Schematic shows how cortical length and thickness were measured. F, fimbria/cortical hem. Nissl-stained coronal sections of control (b,e,h,k) and mutant (c,f,l,l) brains. (b-g) Cortical length of *hGFAP-cre;H1047R* mutant at E14.5 and E16.5 was longer than control; cortical thickness was not different. (h-m) Cortical length of *Nestin-cre;E545K* mutant was longer than control at E16.5 but not at E14.5; thickness was not different at E14.5 but was smaller than control at E16.5. Data are represented as mean±SEM. *, $p<0.05$; **,$p<0.01$; ***,$p<0.001$. Scale bars: 300μm (b,c,e,f,h,i,k,l).

Figure3: *H1047R* and *E545K* mutations differentially affect proliferation, cell density and size in neocortex

(a) Schematic shows area of interest (red box) in E16.5 mouse coronal section, as depicted in c,d,k,m,n,u. (b) Experimental outline of the proliferation and cell cycle exit assays. For labeling index, E14.5 and E16.5 control and mutant brains, harvested after a 1hr BrdU pulse, were processed for BrdU and DAPI staining (c,m). For quit fraction analysis, E16.5 control and mutant brains, pulsed with BrdU at E15.5, were processed for BrdU and Ki67 (k,u). Magnified view of DAPI-stained cortical nuclei shows differences in size and density between controls and mutants (d,n). (e-j,l) E14.5 and E16.5 *H1047R* mutants had similar labeling indices ($BrdU^+$ cells/total $DAPI^+$ cells); E16.5 *H1047R* mutant neocortex displayed reduced cell density ($x10^5$ $DAPI^+$ cells/mm^3 volume), larger nuclear and cell size (μm^2) and similar quit fraction ($BrdU^+Ki67^-$ cells/total $BrdU^+$ cells). (o-q) E14.5 *E545K* mutant neocortex was similar to control in labeling index, cell density and nuclear size. (r-t,v) E16.5 *E545K* mutant showed significantly higher labeling index and quit fraction, reduced cell density, and enlarged cell and nuclear size, compared to controls**.** Data are represented as mean±SEM (e,f,h,i,l,o,p,r,s,v) or as median-centered box-and whisker plots (g,j,q,t); *,$p<0.05$;**,$p<0.001$;***,$p<0.0001$. Scale bars: 50μm (c,d,m,n); 100μm (k,u). See also Figure 3 – figure supplements 1-2.

Figure4: *H1047R* mutant mice display abnormal neocortical layering

(a) Schematics of mouse brain and section; section corresponds to the marked coronal plane; red box in the section marks the area of neocortex (nctx) depicted in the images below. (b-g) and (h-m) correspond to ages E16.5 and P3 respectively. In control cortex, Reelin is in layer I (b), Ctip2 and Tbr1 in deep layers VI and V (d,j), Cux1 in upper layers II-IV (f,l) and NeuN in all matured neurons (h). *H1047R* mutants displayed abnormal distribution of cells for all neocortical layers, observed at E16.5 and P3 (c,e,g,i,k,m). (b',c') Magnified view of Reelin-positive cells in control and *H1047R* mutant. P3 *H1047R* mutant showed enlarged area between ventricular zone (vz) and cortical plate and absence of clear subplate (sp) boundary (h-k). A, anterior; P, posterior; yellow dashed lines, lateral ventricular lining; white dotted lines, pial surface; I-VI, neocortical layers; arrowheads, mispositioned mutant cells. Scale bars: 25μm (b',c'), 50μm (b-i), 150μm (j-o). See also Figure 4 – figure supplements 1-2.

Figure5: *E545K* mutant mice display abnormal neocortical upper layers

(a) Schematics of mouse brain and section; section corresponds to the marked coronal plane; red box marks the area of neocortex (nctx) depicted in the images below. (b-g) and (h-m) correspond to ages E16.5 and P35 respectively. (b-g) Compared to control, in E16.5 *E545K* mutant, layer I appeared normal; deep layers lacked normal arrangement while Cux1-positive cells were dispersed throughout the cortical plate. Extent of dispersion was reduced postnatally (h-m). vz, ventricular zone; yellow dashed lines, lateral ventricular lining; white dotted lines, pial surface; I-VI, neocortical layers; arrowheads, mispositioned mutant cells. Scale bars: 50μm (b-g), 150μm (h-m).

See also Figure 5 – figure supplements 1-3.

Figure6: Birthdating assays demonstrate defects in laminar distribution

(a) Experimental outline of birthdating assays: BrdU was injected at E12.5 and E16.5 and analyzed at P0 (B12.5;P0 and B16.5;P0). Total number of $BrdU^+$ cells at P0 generated at E12.5 and E16.5 (b,j), and total number of $Ctip2^+$ cells (layer V neurons; d,l) were not significantly different between respective controls and mutants, for both *H1047R* and *E545K* lines. (c) Distribution of $BrdU^+$ cells in the neocortex was significantly different between control and *hGFAP-cre;H1047R* mutant for both early and late assays, with more cells residing in the lower cortical plate and white matter instead of mid and upper zones of the cortical plate. (e,m) Total number of layer V neurons in both *H1047R* and *E545K* mutants, born at E12.5 and at E16.5, did not significantly differ from the respective controls; but showed significant difference in their zonal distribution with $Ctip2^+BrdU^+$ cells predominating the lower cortical plate in both the mutants (f,n). Total number of $Cux1^+$ neurons (layers II/III neurons; g,o) was significantly higher in both the mutants compared with the respective controls. The colocalization of Cux1 and BrdU was not significantly different in the *H1047R* mutant and control for both ages (h); but number of $Cux1^+$ cells born at E16.5 was significantly higher in *E545K* mutant than in the control (p). (i,q) Zonal distribution of $Cux1^+$ cells was significantly different between controls and mutants, with more $Cux1^+$ cells residing at the lower portion of the P0 cortical plate. The *H1047R* mutant phenotype is more extreme than the *E545K* mutant. Data are represented as mean±SEM. *,$p<0.05$; **,$p<0.001$; ***, $p<0.0001$

Figure7: PI3K activity acutely modulates epileptic seizures

(a) Schematic shows electrode placement for EEG recordings. LF=Left Frontal, LP= Left Posterior, RF=Right Frontal, RP= Right Posterior. Only 2 electrodes were placed in P35 *Nestin-cre;E545K*. (b) EEG-EMG tracings of *Nestin-cre;E545K* mutant showed bilateral spikes/polyspikes, myoclonic (MC) seizures, fast and slow wave discharges, not associated with movement on video or EMG activity. (c) Generalized (G) and regional (R) spike and wave discharges were observed in *Nestin-creER;E545K* mice. Scale: 1s,1mV. (d,e) Sleep deprivation (SD) enhances epileptiform EEG activity in *Nestin-creER;E545K* mutant. EEG tracings of a *Nestin-creER;E545K* mutant mouse after five hours of normal sleep (Pre SD) and after five hours of total sleep deprivation (Post SD) in the same mouse (d), the mutant showing myoclonic (MC) seizures and isolated regional spikes (R). Power spectrum analysis, representing the frequency distribution for EEG activity over time, also displayed increased activity of the mutant post SD (e). (f) Bar chart showing average number of seizures (SZ) in PTZ-induced P35 *Nestin-cre;E545K* and control over time. (g) Experimental outline for BKM120-PTZ test. (h) Total number of seizures was significantly higher in P35 mutants than controls. Acute administration of BKM120 reduced number of seizures in mutants. (i) Duration of sustained generalized tonic-clonic seizure state (Racine 5), normalized to the total time of test, was significantly longer in P35 *Nestin-cre;E545K* mutants than controls. BKM120 significantly reduced the duration. Data are represented as mean±SEM. *, $p<0.05$; **, $p<0.0001$. See also Figure 7 – figure supplement 1.

Figure8: BKM120 acutely alter PI3K pathway protein profile

(a-g) Graphs show differential protein levels in P35 *Nestin-cre;E545K* mutant and control brains due to different treatments: untreated (-); BKM120; PTZ; BKM120+PTZ. Data are represented as mean±SEM. *, $p<0.05$. Inset shows simplified PI3K pathway; BKM120 significantly regulated the highlighted molecules. See also Figure 8 – figure supplement 1.

Table 1: Summary

Table displays comparison of the key features across different *Pik3ca* genetic models used in this study.

Supplementary file 1: Parameters for motor rotation in LabChart 8 Software

Table shows the list of parameters customized in the stimulator panel dialog box of LabChart 8 Software, in order to randomize the speed and direction of rotation of the motor used for the sleep deprivation study. The stimulation program cycle, comprising segments 1-12, was repeated through the entire duration of the sleep deprivation experiment (i.e. for 5 hours).

Figure Supplements:

Figure 1 – figure supplement 1: Genetic strategy for *Pik3ca* mouse models

(a) Schematic of *PIK3CA* functional domains, highlighting positions of *E545K* and *H1047R* activating mutations. (b) Genetic strategy for tet-activated *H1047R transgenic* mice (Liu et al., 2011): the human H1047R mutation was activated in the combined

presence of cre recombinase and doxycycline (dox). rtTA, reverse tetracycline-controlled transactivator. (c) Genetic strategy for *E545K* conditional knock-in mice (Robinson et al., 2012): exon 9 of PIK3CA gene was replaced by an exon containing *E545K* mutation; and a STOP cassette flanked by loxP recombination sites is introduced in the intron immediately upstream of the exon encoding the transcription initiation site. Cre recombination resulted in removal of STOP cassette, allowing the transcription of the mutant *E545K* allele.

Figure 1 – figure supplement 2: Expression of *cre* lines

Table of *cre* expression for (a) *Nestin-cre*, (b) *hGFAP-cre* and (c) *Nestin-creER* induced by tamoxifen at P0 and P1, using Ai14 and *Rosa26-LacZ* reporter lines.

Figure 1 – figure supplement 3: Neonatal activation of *H1047R* mutation show no effect on brain morphology

hGFAP-cre;H1047R mutant display normal brain morphology, when doxycycline was administered postnatally from P1.

Scale bar: 2mm

Figure 3 – figure supplement 1: Effect of *PIK3CA* mutations on total cell numbers and apoptosis

(a,b) No significant differences in the total cell numbers per cortical column length were observed in *Nestin-cre;E545K* and *hGFAP-cre;H1047R* mutants when compared with their respective control littermates, both at E14.5 and E16.5.

(c,d) TUNEL-positive cell number at E16.5 is significantly lower in *Nestin-cre;E545K* and *hGFAP-cre;H1047R* mutants than the respective controls.

*, p<0.01; **, p<0.001.

Figure 3 – figure supplement 2: *E545K* mutation affects cell size when activated embryonically but not postnatally

(a) Cells of P35 control and *Nestin-cre;E545K* mutant neocortex are marked by pS6. (b) Cell size of P35 *E545K* mutant was significantly larger than that of control littermate. (c) YFP-positive cells of P51 control (*Nestin-creER;YFP*) and mutant *(Nestin-creER; E545K;YFP)*, induced by tamoxifen at P0 and P1 are the cre-recombined cells, DAPI stains the nuclei. (d) Size of these cells was not significantly different between the control and *Nestin-creER;E545K* mutants. Data are represented as median-centered box-and-whisker plot (b,d). white open arrows, control cells; white arrowheads, mutant cells. Scale bars: 100μm (a,c)

Figure 4 – figure supplement 1: Nestin expression in *hGFAP-cre;H1047R* mutant

Nestin-positive radial glial fibres appeared slightly irregular and hyperfasciculated in E14.5 *H1047R* mutant (b) but show progressively dysplastic morphology at E16.5 (d) and P0 (f), compared to respective controls (a,c,e). Yellow boxes (e,f) show broken pia and disrupted radial glial end-feet in the P0 *H1047R* mutant (f). Arrows indicate Nestin-fibers crossed the broken pial surface in the mutant.

Scale bars: 50μm (a,b), 150μm (c-f)

Figure 4 – figure supplement 2: *hGFAP-cre;H1047R* mutant displays distinct white matter dysplasia

Nissl-stained coronal sections of P3 control (a,c,e) and mutant (b,d,f) brains; areas with faint or absence of Nissl stain consist of axon fibre tracts. (a,b) and (c,d) show two comparable antero-posterior planes of section between control and *H1047R (hGFAP-cre;H1047R)* mutant. (a,c) P3 Control sections showed presence of anterior commissure (black arrow), corpus callosum (cc) and hippocampal commissure (hc). *H1047R* mutants lacked corpus callosum (asterisk, b) while other commissures were present (d). Magnified view of neocortex showed expansion of white matter (wm) areas in *H1047R* mutant compared to control (e,f). (e_i) and (f_i) correspond to the dotted boxes in e and f respectively, illustrating presence of increased number of Olig2-positive cells in the expanded white matter area of *H1047R* mutant. The mutant also had an unclear subplate boundary (white dotted line; f, f_i), which is normally seen in the control (sp; e, e_i). CP, cortical plate; vz, ventricular zone.

Scale bars: 50μm (e_i,f_i); 300μm (e,f); 1mm (a-d)

Figure5 – figure supplement 1: Nestin expression in *Nestin-cre;E545K* mutant

Nestin-positive radial glial fibres appeared normal in E14.5 and E16.5 *Nestincre;E545K* mutant (b,d) but subtle abnormalities in the glial end-feet were observed at P0 (asterisks, f), compared to respective controls (a,c,e).

Scale bars: 50μm (a,b), 150μm (c-f)

Figure 5 – figure supplement 2: *Nestin-cre;E545K* mutant displays distinct white matter dysplasia

(a,b) P3 *E545K* mutants (*Nestin-cre;E545K)* had all three major commissures as in control littermates. (c,d) The mutant corpus callosum as well as the corona radiata were thickened compared to controls. c_i, c_{ii}, d_i and d_{ii} correspond to the dotted boxes in (c) and (d) respectively. *E545K* mutants had increased numbers of Olig2-positive cells in an expanded corpus callosum (d_i) and lateral fiber tract (d_{ii}) with respect to the respective controls (c_i, c_{ii}). The subplate in the *E545K* mutant though defined was less packed than the control. CP, cortical plate; cc, corpus callosum; hc, hippocampal commissure; sp, subplate. Scale bars: 50μm (c_i,c_{ii},d_i,d_{ii}); 1mm (a-d).

Figure 5 – figure supplement 3: Astrocytes show no gross dysmorphology in adult *Nestin-cre;E545K* and *Nestin-creER;E545K* mutants

S100 is expressed in astrocytes (a-d). No gross change in morphology or number was observed in the *Nestin-cre;E545K* and *Nestin-creER;E545K;YFP* mutants compared to controls. Insets (a,b) show magnified cells.

Scale bars: 100μm (a-d)

Figure 7 – figure supplement 1: Seizure activity of *E545K* mutants at old age

(a) Experimental outline for ~P180 constitutive (*Nestin-cre;E545K)* mice: Seizures were induced in mice by administering PTZ subcutaneously and then video recorded for 30mins. (b,c) Total number of seizures was not significantly different in P180 *Nestin-cre;E545K* while duration spent by these mutants in severe seizure attacks (Racine 5),

measured as a percentage of the total time of recording, was significantly longer compared to respective controls. (d) Table showing percentage of generalized tonic clonic seizures (GTC SZ) and mean latency (in mins) across different genotypes and age groups. (e,f) In ~P35 *Nestin-creER;E545K* mutants, total seizure number was higher while duration spent in Racine 5, measured as a percentage of the total time of recording, was the same as respective controls. (g,h) In ~P180 *Nestin-creER;E545K* mutants, total seizure number was comparable to the controls but the duration in Racine 5 was different compared to respective controls. *, $p<0.01$; **, $p<0.001$.

Figure 8 – figure supplement 1: RPPA analysis graphs

Protein profile of cortical and hippocampal samples from untreated and treated P35 control and *Nestin-cre;E545K* mutant. Graphs show differential protein levels due to PTZ and BKM120 treatments on control and *Nestin-cre;E545K* mutant.

Mutant allele	H1047R		E545K		
Cre driver	**hGFAP-cre** (dox from E0.5)	**hGFAP-cre** (dox from P1)	**Nestin-cre**	**hGFAP-cre**	**Nestin-creERT2** (tamoxifen @P0/P1)
GoF expression onset	Late embryonic	Neonatal	Early embryonic	Late embryonic	Neonatal
Viability	Lethal by weaning age	Viable	Viable	Viable	Viable
Megalencephaly	✓	X	✓	✓ (intermediate)	X
Hydrocephalus	✓	X	X	X	X
Increased cell size	✓	not tested	✓	X	X
Cortical dysplasia	✓	X	✓	X	X
White matter dysplasia	✓	X	✓	✓ (data not shown)	X
Epilepsy	not tested	not tested	✓	not tested	✓

Table 1

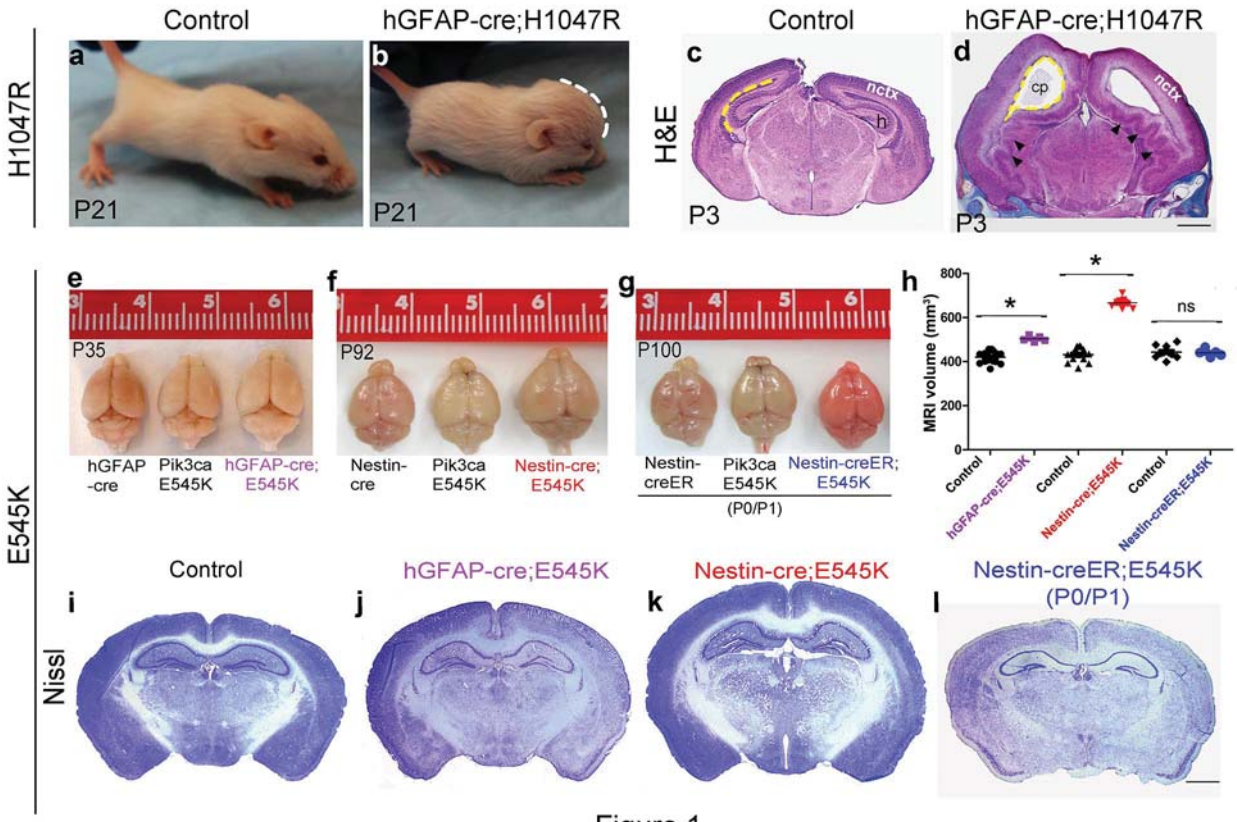
Control
hGFAP-cre;H1047R
Control
hGFAP-cre;H1047R
H1047R
a
b
c
d
H&E
P21
P21
nctx
h
cp
nctx
P3
P3
E545K
e
f
g
h
P35
P92
P100
hGFAP -cre
Pik3ca E545K
hGFAP-cre; E545K
Nestin-cre
Pik3ca E545K
Nestin-cre; E545K
Nestin-creER
Pik3ca E545K
Nestin-creER; E545K
(P0/P1)
MRI volume (mm³)
800
600
400
200
0
*
*
ns
Control
hGFAP-cre;E545K
Control
Nestin-cre;E545K
Control
Nestin-creER;E545K
Nissl
Control
hGFAP-cre;E545K
Nestin-cre;E545K
Nestin-creER;E545K
(P0/P1)
i
j
k
l

Figure 1

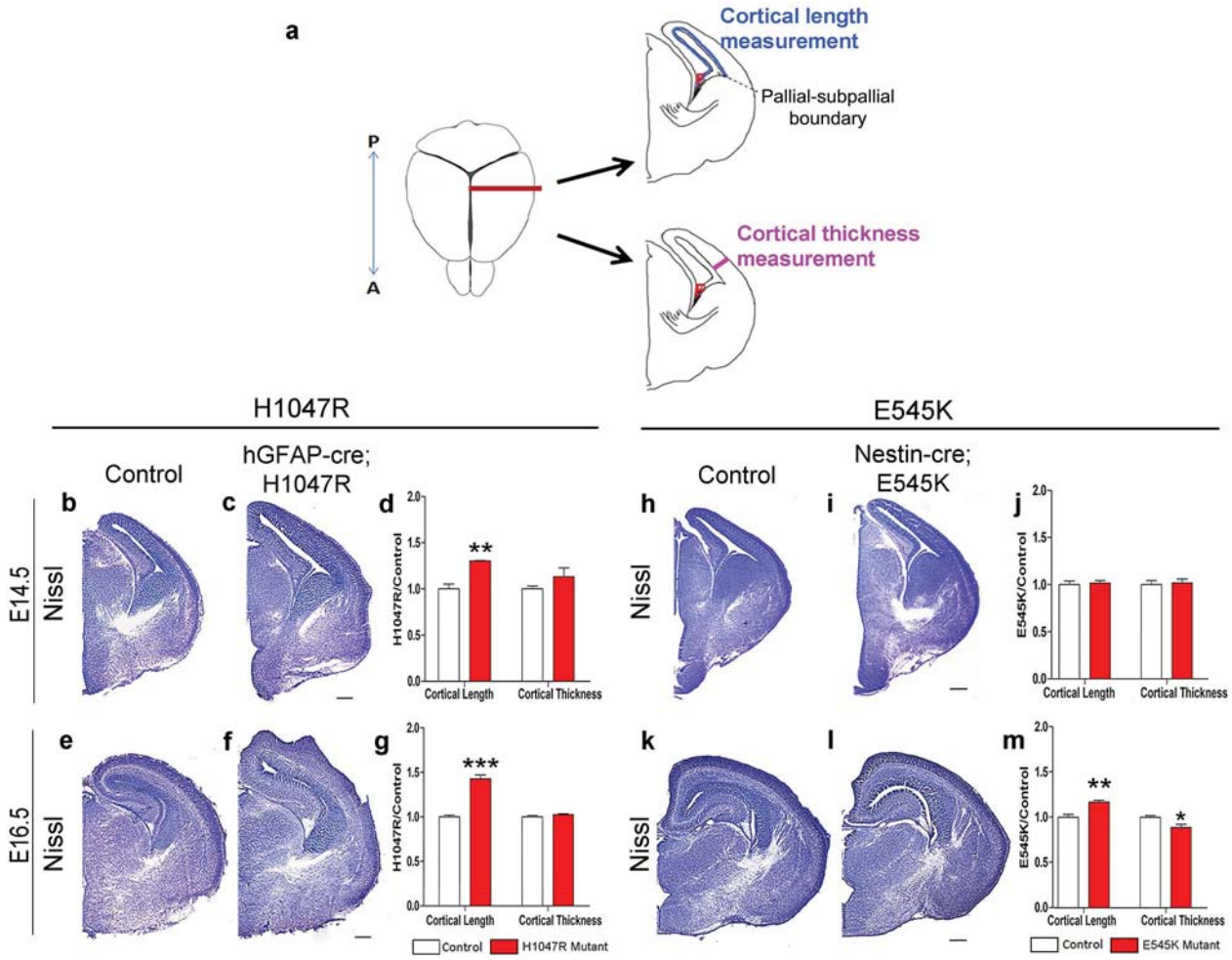
a
Cortical length measurement
Pallial-subpallial boundary
Cortical thickness measurement
P
A
H1047R
E545K
Control
hGFAP-cre; H1047R
Control
Nestin-cre; E545K
E14.5
E16.5
Nissl
b
c
d
e
f
g
h
i
j
k
l
m
H1047R/Control
E545K/Control
Cortical Length
Cortical Thickness
**
***
*
Control
H1047R Mutant
E545K Mutant

Figure 2

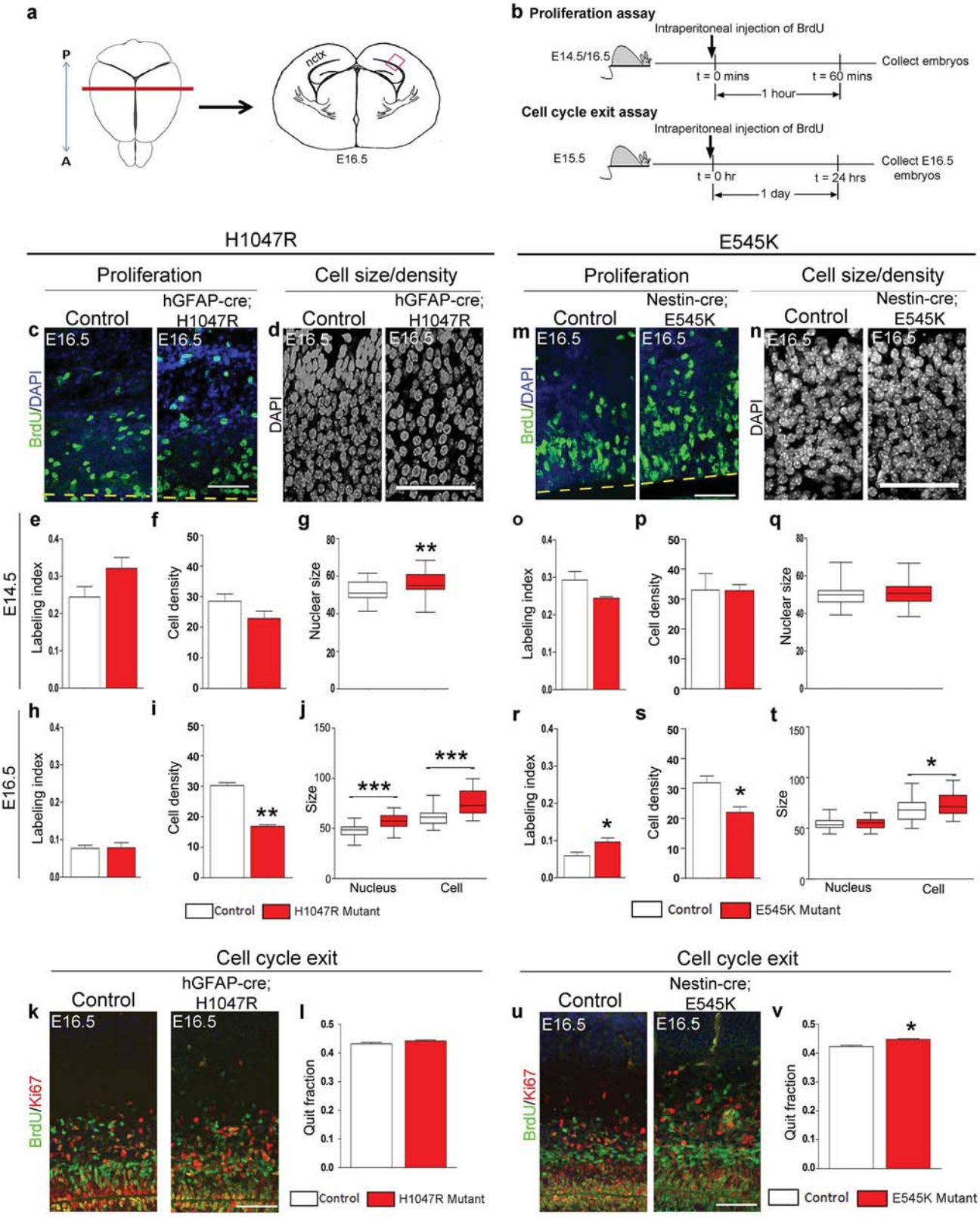
a
P
A
nctx
E16.5
b Proliferation assay
Intraperitoneal injection of BrdU
E14.5/16.5
t = 0 mins
t = 60 mins
1 hour
Collect embryos
Cell cycle exit assay
Intraperitoneal injection of BrdU
E15.5
t = 0 hr
t = 24 hrs
1 day
Collect E16.5 embryos
H1047R
E545K
Proliferation
Cell size/density
Control
hGFAP-cre; H1047R
Nestin-cre; E545K
E16.5
BrdU/DAPI
DAPI
E14.5
E16.5
Labeling index
Cell density
Nuclear size
Size
Nucleus
Cell
Control
H1047R Mutant
E545K Mutant
Cell cycle exit
BrdU/Ki67
Quit fraction

Figure 3

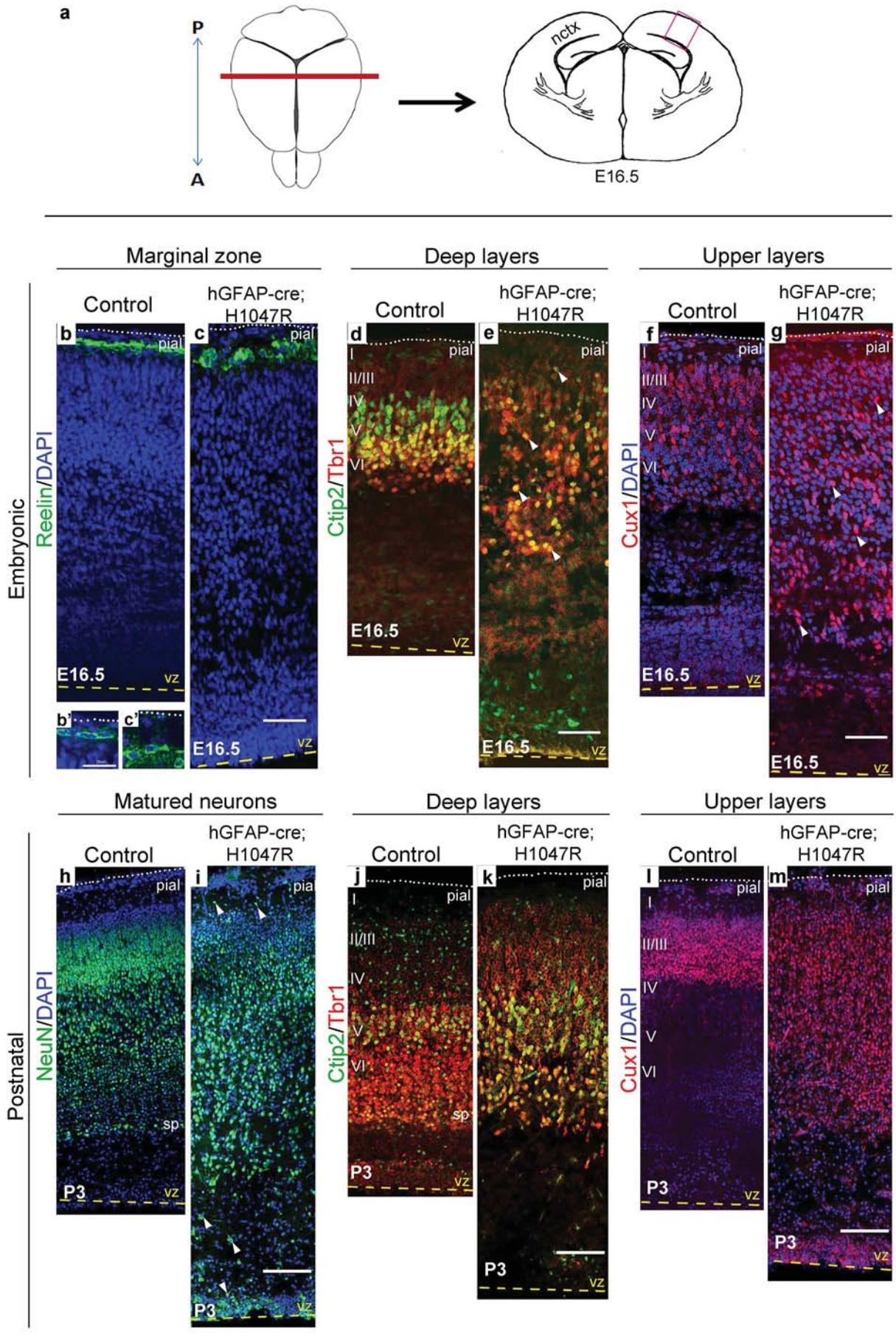
a
P
A
nctx
E16.5
Marginal zone
Deep layers
Upper layers
Control
hGFAP-cre; H1047R
Embryonic
Reelin/DAPI
Ctip2/Tbr1
Cux1/DAPI
pial
E16.5
VZ
Matured neurons
Postnatal
NeuN/DAPI
sp
P3
I
II/III
IV
V
VI

Figure 4

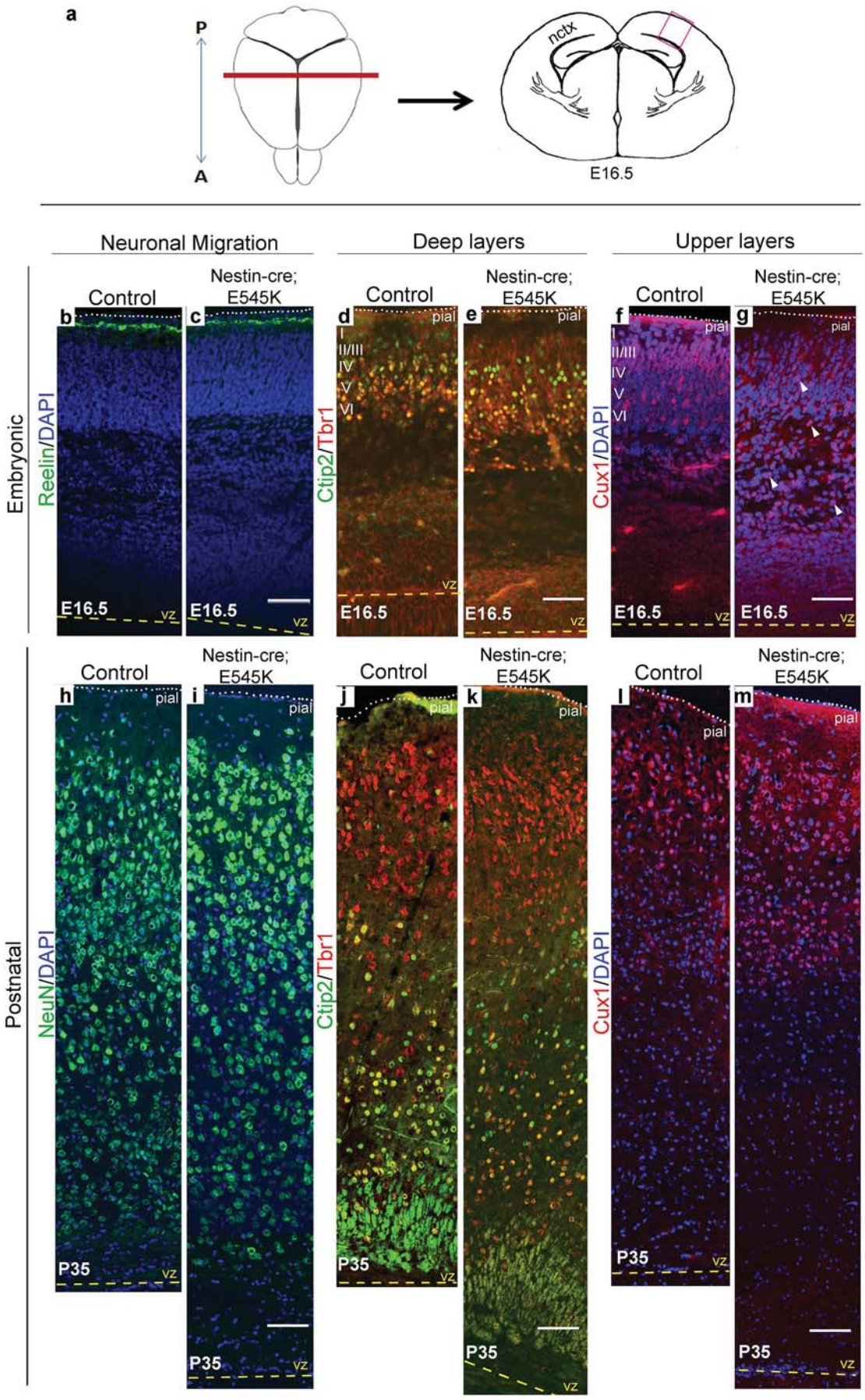
a
P
A
nctx
E16.5
Neuronal Migration
Deep layers
Upper layers
Embryonic
Control
Nestin-cre; E545K
Reelin/DAPI
Ctip2/Tbr1
Cux1/DAPI
pial
vz
I
II/III
IV
V
VI
E16.5
Postnatal
NeuN/DAPI
P35
b
c
d
e
f
g
h
i
j
k
l
m

Figure 5

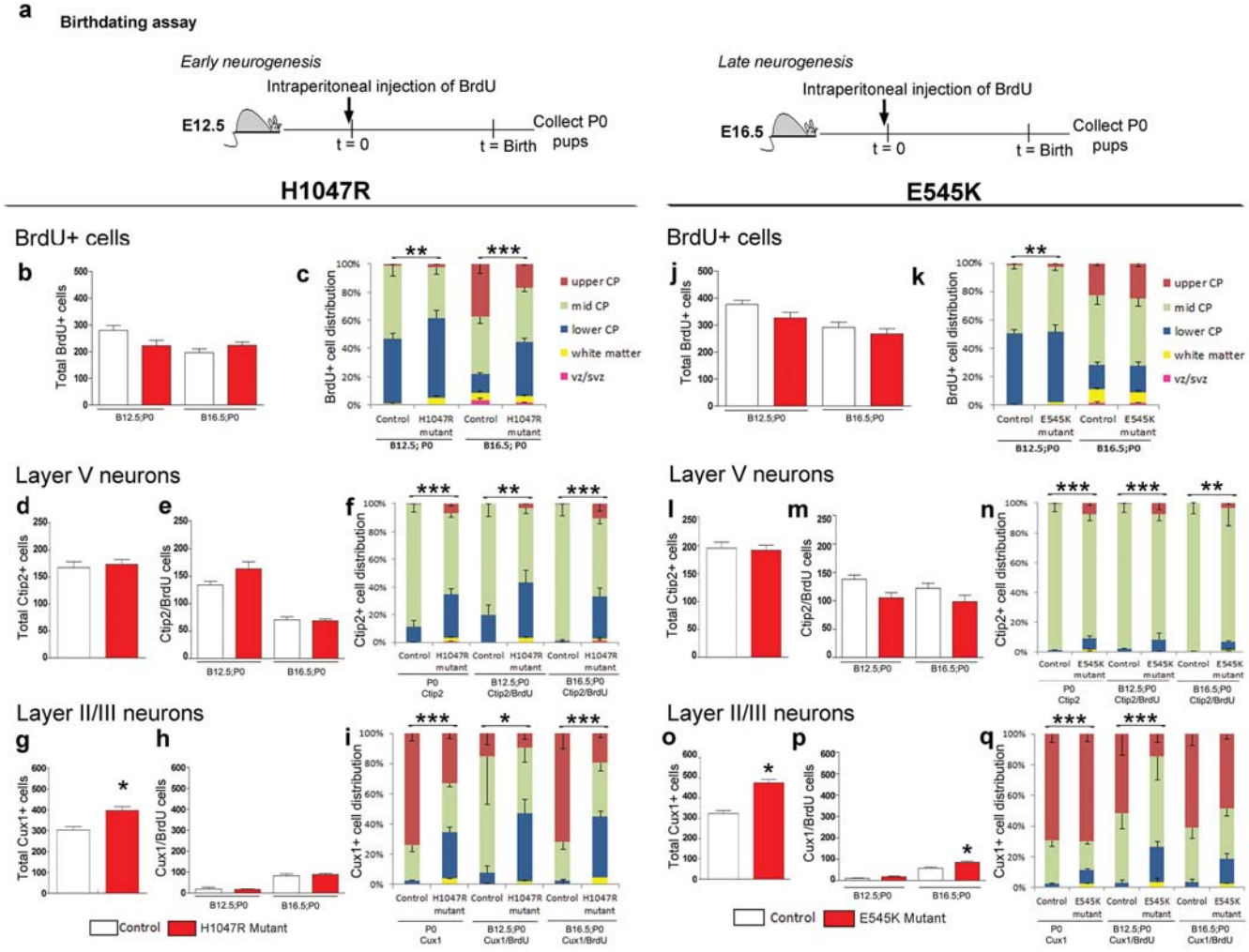
a
Birthdating assay
Early neurogenesis
Intraperitoneal injection of BrdU
E12.5
t = 0
t = Birth
Collect P0 pups
Late neurogenesis
Intraperitoneal injection of BrdU
E16.5
t = 0
t = Birth
Collect P0 pups
H1047R
E545K
BrdU+ cells
Total BrdU+ cells
B12.5;P0
B16.5;P0
BrdU+ cell distribution
upper CP
mid CP
lower CP
white matter
vz/svz
Control
H1047R mutant
E545K mutant
B12.5; P0
B16.5; P0
Layer V neurons
Total Ctip2+ cells
Ctip2/BrdU cells
Ctip2+ cell distribution
P0 Ctip2
B12.5;P0 Ctip2/BrdU
B16.5;P0 Ctip2/BrdU
Layer II/III neurons
Total Cux1+ cells
Cux1/BrdU cells
Cux1+ cell distribution
P0 Cux1
B12.5;P0 Cux1/BrdU
B16.5;P0 Cux1/BrdU
Control
H1047R Mutant
E545K Mutant

Figure 6

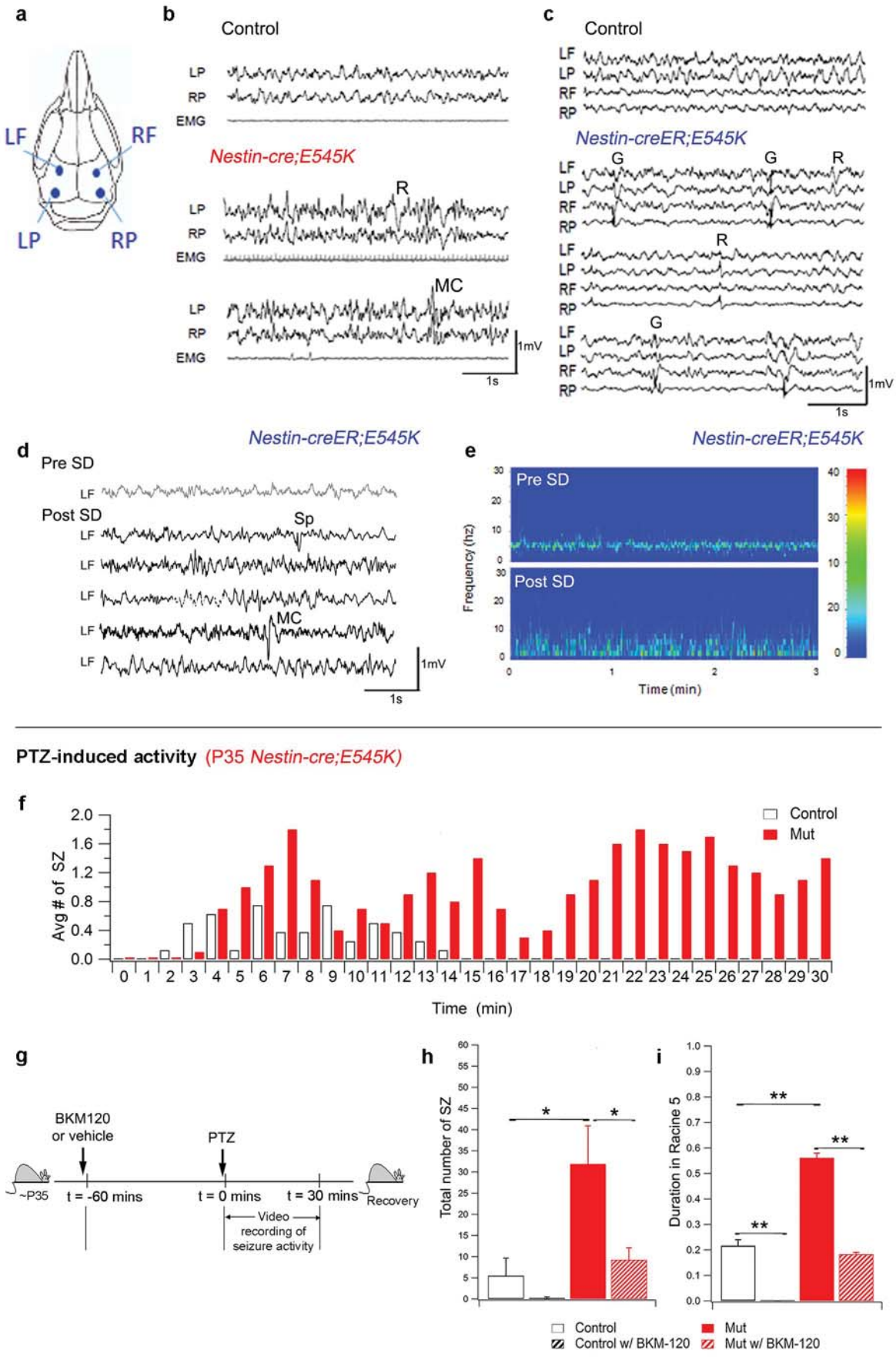
Spontaneous activity
a
LF
RF
LP
RP
b
Control
LP
RP
EMG
Nestin-cre;E545K
R
MC
1mV
1s
c
Control
LF
LP
RF
RP
Nestin-creER;E545K
G
R
1mV
1s
d
Nestin-creER;E545K
Pre SD
Post SD
Sp
MC
1mV
1s
e
Nestin-creER;E545K
Pre SD
Post SD
Frequency (hz)
Time (min)
PTZ-induced activity (P35 Nestin-cre;E545K)
f
Control
Mut
Avg # of SZ
Time (min)
g
BKM120
or vehicle
PTZ
~P35
t = -60 mins
t = 0 mins
t = 30 mins
Recovery
Video
recording of
seizure activity
h
Total number of SZ
i
Duration in Racine 5
Control
Control w/ BKM-120
Mut
Mut w/ BKM-120

Figure 7

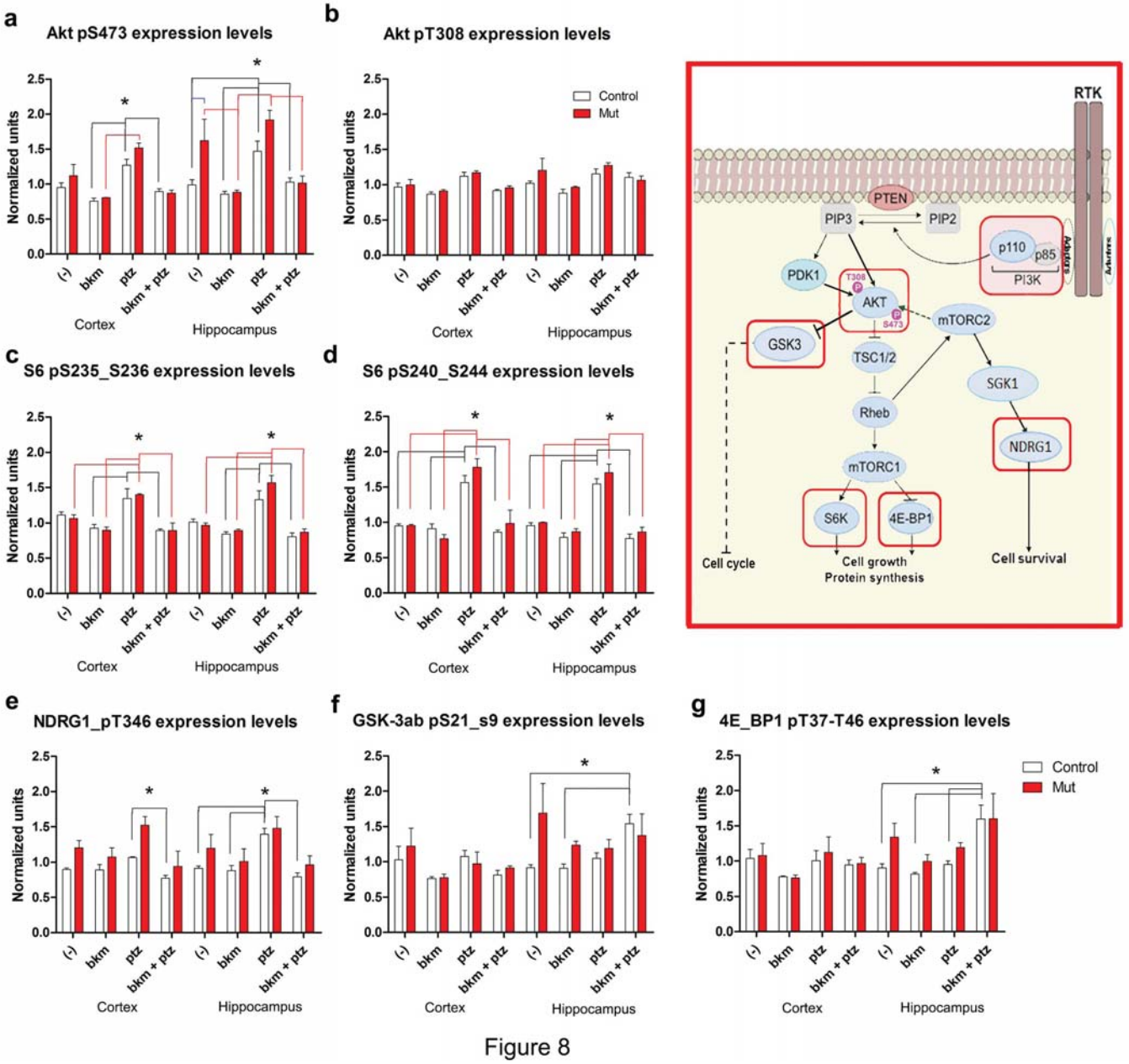
a
Akt pS473 expression levels
b
Akt pT308 expression levels
Control
Mut
Normalized units
(-)
bkm
ptz
bkm + ptz
Cortex
Hippocampus
RTK
PTEN
PIP3
PIP2
p110
p85
PI3K
Adaptors
PDK1
T308
AKT
S473
mTORC2
GSK3
TSC1/2
SGK1
Rheb
NDRG1
mTORC1
S6K
4E-BP1
Cell cycle
Cell growth
Protein synthesis
Cell survival
c
S6 pS235_S236 expression levels
d
S6 pS240_S244 expression levels
e
NDRG1_pT346 expression levels
f
GSK-3ab pS21_s9 expression levels
g
4E_BP1 pT37-T46 expression levels

Figure 8